Rddad, L., Sosnicka, M., Abdelhafid, E., Kraemer, D., Billström, K., Mourad, E., Toummite, A. (2023 online): Fluid evolution and origin of the Tamazert fluorite deposits, Moroccan High Atlas. - Journal of African Earth Sciences, 104856.

https://doi.org/10.1016/j.jafrearsci.2023.104856

Fluid evolution and origin of the Tamazert fluorite deposits, Moroccan High Atlas

Larbi Rddad[1], Marta Sośnicka[2], Essalhi Abdelhafid[3], Dennis Kraemer[4.5], Kjell Billström[6], Essalhi Mourad[3], Abdeslam Toummite[3]

1. Department of Physical Sciences, Earth and Planetary Division, Kingsborough Community College of the City University of New York, 2001 Oriental Boulevard, Brooklyn, New York, NY 11235-2398, USA

2. GFZ German Research Centre for Geosciences, Telegrafenberg, D-14473 Potsdam, Germany

3. Laboratoire de Géologie Appliquée, Université Moulay Ismaïl, Faculté des Sciences et Techniques, BP. 509, Boutalamine, 52000, Errachidia, Morocco

4. Department of Physics and Earth Sciences, Jacobs University Bremen, Campus Ring 1, 28759 Bremen, Germany

5. Current address: Federal Institute for Geosciences and Natural Resources, Stilleweg 2, 30655 Hanover, Germany

6. Department of Geological Sciences, Swedish Museum of Natural History, Box 50 007, SE-104 05 Stockholm, Sweden

Abstract

This study focuses on the origin of fluorite ore deposits that are associated with the Eocene alkaline igneous suite of the Tamazert complex in the Moroccan High Atlas. Based on field observations and mineralogy, two major ore styles were identified: 1) a disseminated purple fluorite in aegirine-rich nepheline syenites (stage 1) and 2) a banded purple-white fluorite ore in karstic cavities and veins hosted in the Jurassic carbonate (stage 2). Both fluorite mineralization stages are commonly accompanied by

calcite. The distribution of fluorite deposits at the peripheries of syenite and the surrounding Jurassic carbonates suggests the development of long-lived hydrologic systems around the shallow intrusion. Based on fluid inclusion, Rare Earth Elements and Yttrium (REY), and C-O isotopic constraints, this study reveals that different fluid systems were responsible for the deposition of fluorite ores in and around the Tamazert alkaline igneous complex. The disseminated interstitial fluorite precipitated from a F-rich magmatic-hydrothermal fluid, which exsolved from the highly evolved alkaline-silicate melt and was subsequently altered by Na-Ca metasomatic brines. Vein-type fluorite deposits hosted in the Jurassic carbonates precipitated from low salinity (1.6-8.5 wt.% NaCl equiv.) and heated (T_h = 118-157°C) meteoric fluids, which migrated in response to the heat flow around the shallow intrusion. Fluid cooling, fluid interaction with Jurassic carbonates, and pressure fluctuations were the most important fluorite deposition mechanisms. The evolved melt provided F and REY for the interstitial fluorites, whereas meteoric fluids leached F^- from syenites and other F-bearing igneous rocks. Based on the fractionation pattern, the REY inventory of the vein fluorites was acquired by interaction of meteoric fluids with Jurassic carbonates.

Keywords: fluorite, ore deposits, Moroccan High Atlas, Tamazert complex, fluid inclusions, REY, C-O isotopes

1- Introduction

Many economic fluorite deposits are either associated with alkaline-peralkaline igneous rocks (Alvin et al., 2004; Öztürk et al., 2019; Salvi et al., 1990; Sami et al., 2017; Simonetti and Bell, 1995) or share attributes akin to Mississippi-Valley-Type (MVT) ore deposits (Bouabdellah et al., 2016; González-Partida et al., 2003; Munoz et al., 2005; Nadoll et al., 2019). The origin of fluorite deposits spatially associated with igneous cupolas remains controversial as their formation time span may not necessarily correspond to the timing of the magmatic event. Consequently, ore deposits around intrusions may be associated with different fluid systems, which can be directly or indirectly linked to magmatism, or which post-date the magmatic activity (e.g., Lüders et al., 2009; Sizaret et al., 2004; Wang et al., 2020).

Nevertheless, magmatic-hydrothermal fluids are commonly responsible for the precipitation of fluorite and rare metal-bearing minerals in intrusion-related settings (e.g., Buhn et al., 2002; Deng et al., 2015; Öztürk et al., 2019; Sami et al., 2022; Wang et al., 2020; Williams-Jones et al., 2000). Numerous fluid inclusion studies revealed that basinal brines were responsible for the precipitation of the MVT fluorite mineralization, e.g., in the French Massif Central and the North German Basin (e.g., Munoz et al., 1999; Munoz et al., 2005; Nadoll et al., 2019; Sośnicka and Lüders, 2019), whereas modified meteoric fluids played an essential role in the genesis of rift-related fluorite deposits, e.g., in the Hansonburg district and other Rio Grande rift deposits (Hill et al., 2000; Partey et al., 2009; Rowan et al., 1996; Zappettini et al., 2017). Some studies suggest that fluorite mineralization, spatially and temporally linked to alkaline igneous plutons, requires the interaction of at least two fluid systems. For example, according to Simonetti and Bell (1995), the mixing of carbonatite-derived fluid with groundwaters contributed to the deposition of the giant Amba Dongar complex in India. An interplay of two fluid systems, i.e., orthomagmatic fluids and externally derived formation waters, has also been inferred as a precipitation mechanism for fluorite in breccia-hosted fluorite-bastnaesite deposits linked to syenite intrusions in the Gallinas Mountains, New Mexico (Williams-Jones et al., 2000). In Tunisia, the MVT-type ore deposits in the Zaghouan province, major producers of fluorite ore, are formed from the basinal fluids in relation to the Alpine orogeny (Bouhlel et al., 1988; Jemmali et al., 2019; Souissi et al., 1997). In Morocco, economic fluorite deposits (e.g., El Hammam, Aouli) are spatially associated with magmatic intrusions, which were emplaced during the Central Atlantic Magmatic event. The basinal brines, rather than magma-derived fluids, were proposed as the primary fluids responsible for fluorite precipitation of these ore deposits (El Hammam and Aouli deposits) based on fluid inclusion and REY data (Bouabdellah et al., 2010; Margoum et al., 2015). Therefore, fluorite deposits are characterized by different sets of fluid characteristics depending on the ore style, geologic setting, and ore-forming processes.

The abundance of fluorite-bearing ore veins hosted in the Tamazert alkaline igneous complex, as well as the adjacent Jurassic carbonates in the Moroccan Central High Atlas, raises the question of whether

the F-rich fluids were primarily derived from the evolving alkaline magma or were supplied from external sources and acquired fluorine due to a long-lasting migration and leaching of the igneous Tamazert complex. The evolution of fluid systems around the Tamazert igneous body is poorly understood and it is not clear which fluid types were responsible for the ore formation. Previous studies have shown that syenites and pegmatites of the Tamazert complex are enriched in fluorine and suggested that F-rich and Ca-poor orthomagmatic brine likely exsolved from alkaline magma at high temperatures (<500°C) and mixed with Ca-rich meteoric fluids at shallow depths (Bouabdellah et al., 2010; Salvi et al., 2000). Based on preliminary petrographic information, Achmani (2017) suggested that fluorite veins precipitated by the interaction of the F-rich fluid with Jurassic carbonates at the Bou Izourane fluorite deposit, located near the Tamazert complex. However, there is a lack of convincing scientific support for this hypothesis. Hence, this contribution aims to constrain the types and sources of the ore-forming fluids and the mechanism(s) of fluorite precipitation.

2. Geological setting

The Moroccan Atlas segment consists of the NE-SW-trending Middle Atlas and the ENE- WSW-trending High Atlas (Fig. 1). The High Atlas is marked by large-scale folds dominated by ENE-WSW-trending ridges, separated by wide synclines (Fig. 1). It consists of Mesozoic to Cenozoic sedimentary rocks covering the Paleozoic basement, which was deformed and metamorphosed during the Hercynian orogeny (Piqué and Michard, 1989; Yaagoub et al., 2022 and references therein). The Paleozoic succession, mainly composed of siliciclastic rocks, crops out in the Mouguer, Bou Dahar, and Tamlet inliers (Fig. 1). Two major tectonic events occurred in the High Atlas region: Jurassic rifting and Cenozoic tectonic inversion. The first event started with the Triassic rifting during the opening of the Central Atlantic Ocean and the formation of the Tethys Ocean (Ellero et al., 2020; Frizon de Lamotte et al., 2009; Laville, 1988). This rifting reactivated the Hercynian NE-SW-trending faults entrenched in the Paleozoic basement (Karaoui et al., 2022 and references therein; Laville, 1985; Laville et al., 2004). As a result, the Triassic rift basins were formed and were subsequently filled with detrital siliciclastic sediments and thick evaporitic sequences.

During this tectonic event, tholeiitic basaltic flows were emplaced and intercalated within the Triassic red beds (Du Dresnay, 1987; Yaagoub et al., 2022 and references therein). This magmatism represents the first magmatic event, known as the Central Atlantic Magmatic Event. Following the deposition of the Triassic series was the development of the Liassic carbonate platform, which evolved into marls alternating with limestones (Du Dresnay, 1979; El Ouali et al., 2021 and references therein). This change in sedimentation marked the Middle Liassic-Middle Jurassic rifting (Ellouz et al., 2003; Sadki and Sha, 2018 and references therein; Warme, 1988). The second magmatic event occurred during the Middle Jurassic-Early Cretaceous time in response to the crustal extensional tectonic activity (Essaifi and Zayane, 2018 and references therein; Frizon de Lamotte et al., 2009; Zayane et al., 2002). This magmatic event is represented by the emplacement of basaltic, alkaline lavas and mafic, gabbroic igneous rocks that intruded the ENE-WSW-trending ridges (Essaifi and Zayane, 2018 and references therein; Jenny et al., 1981; Laville and Harmand, 1982; Laville et al., 2004; Laville, 1985; Lhachmi et al., 2001; Zayane et al., 2002). At the end of the Middle Jurassic (late Bajocian-Bathonian), a regional uplift occurred (Saddiqi et al., 2009), and a marine regression led to the deposition of continental red beds (Charrière and Haddoumi, 2016; Jenny et al., 1981).

The collision between the African and European plates led to tectonic inversion (Alpine orogeny) (Ellero et al., 2020; Frizon de Lamotte et al., 2009; Tapponier, 1977). Two major compressional tectonic events with intermittent quiescent periods were recognized (Frizon de Lamotte et al., 2009). The first Atlasic tectonic event occurred during the Middle-Late Eocene, followed by a calm period during the Oligocene-Miocene (Frizon de Lamotte et al., 2009). The second shortening Atlasic event, responsible for the uplift and the formation of the High Atlas, occurred during the Late Miocene (Frizon de Lamotte et al., 2009). During the Alpine orogeny, a third magmatic event took place in the Eocene (Bouabdellah et al., 2010; Tisserant et al., 1976). During this magmatic event, the Eocene alkaline magmatic rocks crystallized from magma derived from the laterally flowing mantle plume of the Canary Islands, which was generated due to the delamination of the subcontinental lithosphere in response to the African-European collision (Bouabdellah et al., 2010; Duggen et al., 2009). The asthenosphere uplift (thermal anomaly) is inferred

under the Central High Atlas during the middle to late Miocene. This thermal doming anomaly is related to the lithospheric thinning and a shallow mantle plume emplaced during a period of relatively tectonic quiescence (Missenard et al., 2006; Teixell et al., 2005). This magmatic event formed the igneous rock complex of Tamazert, located north of the Central High Atlas (Fig. 1). Kchit (1990) suggested a syntectonic emplacement of the Tamazert intrusion along crustal fractures created by the same NE-SW sinistral shearing in relation to the convergence between the African and European plates. To account for the diverse igneous rocks of the Tamazert complex (Figs. 2-3), Bouabdli et al. (1988) and Kchit (1990) proposed fractional crystallization of a common parental magma of nephelinitic or monchiquitic composition. Recent works have suggested successive melting of the compositionally heterogeneous mantle, fractional crystallization of magmas (Marks et al., 2008; 2009), magma contamination by assimilation of Jurassic limestones (Bouabdellah et al., 2010; Marks et al., 2009), as well as late-stage fluid-rock interactions (Marks et al., 2009) to explain this diversity.

The Moroccan High Atlas range hosts numerous ore deposits and prospects (Ovtracht, 1978), which are mainly located near the Paleozoic paleohighs (e.g., Mougueur, Bou Dahar, Fig. 1), near the Jurassic magmatic intrusions and diapirs (e.g., Tirrhist, Ali Ou Daoud, Tazoult, Fig. 1), and close to the borders of sedimentary basins (e.g., Tigrinine-Taabast) (Fig. 1) (Rddad, 2021; Rddad and Mouguina, 2021). The Central High Atlas hosts Pb-Zn (Fe, Cu) deposits in the vicinity of the Jurassic igneous intrusions (e.g., Ali Ou Daoud Pb-Zn-Fe ore deposit, Mouguina, 2004; Rddad et al., 2018) or intimately associated with these igneous rocks (e.g., Tirrhist, Mouguina, 2004). These deposits were formed during the Jurassic to Early Cretaceous time in direct or indirect relation to Jurassic magmatism (Mouguina, 2004; Rddad et al., 2018). Other major Pb-Zn (± Ba, Sr) ore deposits hosted in Jurassic carbonates include the Bou Dahar (Adil et al., 2004; Rddad and Bouhlel, 2016) and Tigrinine Taabest (Rddad, 2021). These Mississippi-Valley-Type ore deposits were formed during the Eocene-Miocene times and are related to the Alpine orogeny (Bouabdellah and Sangster, 2016; Rddad, 2021; Rddad and Bouhlel, 2016). Ore deposits centered around the Tamazert

complex are set apart from other deposit types in the region due to their proximity to the Eocene alkaline igneous massif and their commodity, i.e., fluorite.

3. Local Geology

The study area is located in the northern part of the Central High Atlas, about 30 km NW of Rich City (Fig. 1). In the studied area of about 48 km^2, Jurassic carbonates and marls crop out at the surface, and they discordantly overlie the Paleozoic basement (Figs. 2-3). The latter is primarily composed of schists and amphibolites, siliciclastics in the area (Emberger, 1965; Ouanaimi et al., 2018). The Jurassic sequence begins with the Hettangian-Sinemurian unit (200-500 m thickness), consisting of massive dolomitic limestone (Fig. 4), which is followed by the Pliensbachian unit (~ 450 m), composed of alternating decimeter-sized beds of limestone and marl (Fig. 4) (Achmani, 2017; this study). The third Toarcian-Aalenian unit (~300 m) consists of limestone layers alternated with marl beds (Fig. 4). These Triassic-Jurassic series were intruded by alkaline igneous rocks, which include syenites, pegmatites, carbonatites, and lamprophyres (Figs. 2 and 3) (Bouabdellah et al., 2010; Marks et al., 2009).

The alkaline igneous rocks are part of the NE-SW-trending elliptical Tamazert alkaline complex, 17 km long and more than 5 km wide (Bouabdellah et al., 2010; Bouabdli et al., 1988). The nepheline syenites of the Tamazert complex crop out in the western part of the investigated area (Figs. 2-5), whereas the eastern part is dominated by older Liassic carbonate-bearing sedimentary sequences (Figs. 2-5). The nepheline syenites contain alkali feldspar, aegirine, and nepheline feldspathoid with subordinate plagioclase, amphibole, and disseminated fluorite. Syenite consists of aegirine, alkali feldspar, plagioclase, alkali feldspar, calcite, quartz, and disseminated fluorite (Fig. 6a-b). Pegmatite occurs as irregular, metric-sized bodies or pockets at the periphery of syenite/nepheline syenite and represents the late stage of magma evolution.

West of Tabeja (point 5 in Fig. 3), the contact between the syenite intrusion and the Jurassic carbonates is marked by a poorly developed skarn, which consists of fibro-radial wollastonite, abundant small crystals of calcite and clinopyroxene (Fig. 6c-d). At the Bou Imtessene, the skarn consists of pyroxene, fluorapatite, garnet, titanite, mica, alkali feldspars, plagioclase, disseminated fluorite, and abundant calcite (Figs. 6e-f and 7a-b). Lamprophyre rocks are abundant in the studied area and form a network of N-S- to NNE-SSW-trending dikes that crosscut syenites (Fig. 7d) and Jurassic rocks (Figs. 2 and 3). These lamprophyre dikes are 0.5-6 m wide (Fig. 7d) and extend over 2 km (Fig. 2). They have a fine-grained texture consisting mainly of alkali feldspar, clinopyroxene (aegirine), rare orthopyroxene, zircon, and disseminated fluorite (Bouabdli et al., 1988). Carbonatite rocks crop out about 6 km NW of the Bou Imtessene deposit and are predominant further to the north, where they occur as NE-SW-trending igneous rock units (Fig. 2) and cut through the syenite, the lamprophyre, and the Jurassic limestone (Bouabdellah et al., 2010; Marks et al., 2009). Based on structural relationships, Al-Haderi et al. (1998) and Kchit (1990) suggested that nepheline syenites and monzonites formed simultaneously, followed by the emplacement of various intrusive and extrusive dikes of lamprophyre and carbonatites, among other igneous rocks. The nepheline dikes and carbonatites that post-date syenite have radiogenic ages of 35±3 Ma (Klein and Harmand, 1985) and 39±4 Ma (Agard, 1977), respectively. Moreover, Tisserant et al. (1976) determined an Rb/Sr age of 44±4 Ma for monzonites.

Field observations in the study area reveal three important systems of faults and fractures (Achmani, 2017; this study) (Figs. 3-5). The N-S-trending fault system is predominant in the area and consists of reverse faults with a sinistral strike-slip component, dipping at 70 to 90º towards the east. This fault system shared a similar orientation as the lamprophyre dikes. The ENE-WSW- trending fault system consists of subvertical faults that are frequent in the NW and SE of the studied area. Besides these major fault systems, less representative fault sets oriented NE-SW are also identified in the area. The ENE-WSW- and NE-SW-trending fault sets host fluorite ore (Figs. 3 and 5). The N-S faults that controlled the emplacement of lamprophyre dikes often offset the NE-SW-trending fluorite-bearing faults/fractures (Achmani, 2017; this study). These aforementioned faults were formed and/or reactivated during the Eocene-Oligocene

transpressive-transtensional tectonic regime shift when the Tamazert igneous rocks were emplaced (Bouabdellah et al., 2010). Following this tectonic regime shift, the Alpine tectonic phases caused the uplift of the present-day Tamazert complex and the simultaneous formation of the narrow anticlines separated by large synclines.

4. Ore geology

The Jurassic carbonate and Eocene igneous rocks of the Tamazert complex host several fluorite deposits: Bou Imtessene, Tabeja, Bou Izourane, and Bou Kharouba (Figs. 2-3). These ore deposits were discovered by the "La Society Global Des Mines" company in 2004. The Jurassic carbonate-hosted ore deposits are the economically profitable with an estimated annual production of fluorite of 11,000 tonnes and an estimated reserve of 150,000 tonnes at grades of 50% CaF_2. Bou Imtessene fluorite deposit, formed at the peripheries of the syenite intrusion (Fig. 3, Fig. 7a-c), is currently of no economic interest. The Bou Imtessene, Tabeja, and Bou Izourane fluorite deposits are the focus of this study (Figs. 3-5).

In Bou Imtessene deposit, fluorite is disseminated within syenite and corresponds to the earliest recognized fluorite generation (F-1) (Figs. 7b and 6e-f). Vein-hosted fluorite (F-1a) and calcite (Ca-1a) crosscutting the syenite (Fig. 7c) belong to a relatively later substage of the syenite-related fluorite mineralization. The currently exploited structurally-controlled fluorite veins, which are hosted in the Jurassic carbonates (Fig. 8a-c), are considered the second generation of fluorite (F-2). The latter generation (F-2) is also found in brecciated zones and karstic cavities (Fig. 9a-b) of variable dimensions (Achmani, 2017; this study). The ore-bearing faults display similar NE-SW orientation (Fig. 8b) as those of the Tamazert igneous complex rock units.

5. Sampling and methodology

A suite of representative samples of two generations of fluorite mineralization (F-1and F-2) was collected from the syenite and the Jurassic carbonates. The codes used for the samples' references are IM (Bou

Imtessene), TJ (Tabeja), and BZ (Bou Izourane). The fluorite and calcite samples were collected from the syenite of the Bou Imtessene deposit (IM samples) (Fig. 3, Table 1). The sampling of carbonate-hosted fluorite mineralization and calcite from fractures and karsts in the carbonate sequence has been performed at or near the ore deposits of Tabeja (TJ samples) and Bou Izourane (BZ samples) (Fig. 3, Table 1). The syenite, carbonatite, lamprophyre, pegmatite, Jurassic marls, limestone, and skarn rocks were collected at different sites near the studied ore deposits (Fig. 3, Table 1).

5.1. Rare earth elements and Yttrium (REY) geochemistry

REY and other trace elements were analyzed with quadrupole ICP-MS at the Geochemistry Lab at Jacobs University Bremen, Germany. All reagents used for sample decomposition were of pure grade, and the purity of all reagents was verified by blank measurements. The powdered country rocks and mineral separates (fluorite and calcite) were dried at 110°C for 24 h and then weighed into acid-cleaned PTFE digestion vessels of a Picotrace DAS acid digestion system (Picotrace GmbH, Bovenden, Germany). The digestion was conducted in closed vessels with 3 ml of concentrated HF and 3 ml of concentrated $HClO_4$ at elevated temperatures and pressures. After digestion and subsequent evaporation of the acid mixture to incipient dryness, the samples were taken up in 0.5 M HNO_3 and, following further dilution, analyzed with a Perkin-Elmer NexION 350x ICP-MS. 1 ppb of Ru, Rh, Re, and Bi was used for internal standardization. The certified reference materials J-Do1 (dolomite, Geological Survey of Japan) and BHVO-2 (basalt, USGS) were used for quality control of the analysis. Deviations from published literature values (Dulski, 2001) were <<5 % for all reported analytes except for Pr, which we measured as 7.2% lower.

5.2. C-O isotope analyses

The C-O isotope analysis was carried out at the Stable Isotope Mass Spectrometer facility at the Memorial University of Newfoundland, St. John's, Canada. Mineral separates for C and O isotope analyses were prepared under a binocular microscope by handpicking or using a micro-drill. The analysis of carbon and oxygen stable isotopes was performed on samples of the Jurassic limestone host rock (n = 2), altered limestone (n = 4), carbonatite (n = 3), skarn rocks of the contact zone (n = 5), and calcite (n =

9). One mg of powder sample was placed in a vial and heated to 50°C in an inert atmosphere for 5 minutes. Samples were, then, manually injected with 0.05 ml of 100% phosphoric acid using a syringe and needle. The carbon isotopic compositions were reported in delta notation ($\delta^{13}C$) relative to V-PDB, and the oxygen isotopic compositions were reported in delta notation ($\delta^{18}O$) relative to V-PDB and V-SMOW. The precision of carbonate analyses is better than ±0.1‰ for both $\delta^{13}C$ and $\delta^{18}O$. The precision was determined by repeated measurements (n = 4) of NBS-19 ($\delta^{18}O_{VPDB}$ = −2.20‰, $\delta^{13}C_{VPDB}$ =+1.95‰), CBM ($\delta^{18}O_{VPDB}$ = +22.06‰, $\delta^{13}C_{VPDB}$ = + 0.75‰), and MUN-CO-1 ($\delta^{18}O_{VPDB}$ = +17.10‰, $\delta^{13}C_{VPDB}$ = −21.02‰).

5.3. Microthermometry and Raman spectroscopy

Microthermometric and Raman spectroscopic analyses were carried out at the GFZ German Research Centre for Geosciences in Potsdam, Germany. A fluid inclusion study was carried out on nine samples of fluorite and one sample of calcite. Doubly polished, ~190 µm thick wafers were examined for fluid inclusions hosted in fluorite and calcite samples. Microthermometric measurements were performed using a FLUID INC. adapted to a USGS heating/freezing system mounted on a BX50 Olympus microscope. The USGS stage was calibrated with synthetic fluid inclusion standards supplied by Synflinc. The accuracy is ±0.1°C for T_m(ice) and ±1.7°C for T_h above 350°C. The salinities of aqueous fluid inclusions are expressed in wt. % NaCl equiv. and were calculated using the Microsoft Excel spreadsheet HOKIEFLINCS-H_2O-NaCl (Bodnar, 2003; Steele-MacInnis et al., 2012; Sterner et al., 1988). Raman spectroscopic analyses were performed using a LabRAM HR Evolution (Horiba Scientific) Raman spectrometer equipped with the Nd:YAG green laser source with excitation radiation of 532 nm. The silicon standard (520 cm^{-1}) was used for internal calibration. Raman spectra of the solid phases were acquired in the spectral range between 200 and 1300 cm^{-1}, and a 2x20s acquisition time was used. Spectral data from this study were compared with reference data from the RRUFF database (Lafuente et al., 2015).

6. Results

6.1. Paragenetic sequence

The earliest recognized mineralization stage is represented by disseminated fluorite (F-1), which occupies the interstices in the altered syenite (Fig. 6e-f, samples IM3, IM11). Fluorite (F-1) is associated with calcite (Ca-1) and is hosted in the endoskarn (Fig. 6e-f). Later vein fluorite (F-1a) occurs in the NW- and NE-trending fractures, often forming irregular veins that crosscut syenite and the skarn rocks (Fig. 7b-c). The primary paragenetic sequence for fluorite-bearing deposits at the peripheries of the igneous Tamazert complex (altered syenite, skarn), excluding rock-forming and alteration minerals, can be summarized as follows: disseminated purple and white fluorite (F-1), disseminated calcite (Ca-1), and fluorite-calcite (F-1a, Ca-1a) veins.

In Bou Izourane and Tabeja deposits, the ore consists mainly of fluorite (F-2) associated with subordinate calcite (Ca-2). Fluorite (F-2) ore precipitated primarily in open-space fillings (Figs. 5, 8, and 9, Table 1) and is hosted in the Hettangian-Sinemurian carbonates and the Pliensbachian marl-limestone series (Fig. 4). The fluorite-bearing ore zones developed in limestones in the vicinity of the Bou Izourane fault zone (Figs. 5 and 8b-c). Fluorite ores display sharp contact with the host rock (Fig. 8a). Vein fluorite reaching up to 4 m-thickness and 200 m in length is also observed close to the fault zone (Figs. 3 and 5). The ore-bearing veins run parallel to the NE-SW- to NEE-SWW-trending faults (Fig. 8b). The latter faults are linked to satellite N-S to NNE-SSW faults, where fluorite ore was encountered in brecciated zones (Fig. 8c). In these zones, fluorite (F-2) and calcite (Ca-2) cement the Jurassic carbonate-derived breccia clasts (Fig. 8c). The fluorite (F-2) often occurs as euhedral purple coarse crystals intergrown with calcite (Ca-2) (Fig. 8d). Locally, the ore displays a color zonation with mm-thick alternating bands of purple fluorite (F-2) and white fluorite (F-2), referred to as “banded purple-white fluorite”. This banded fluorite is associated with calcite (Ca-2) and iron oxides (Figs. 6g and 8d). The euhedral plain white fluorite (F-2) is also intergrown with Fe oxides and purple fluorite (F-2) (Fig. 8e). The post-ore calcite (Ca-3) occurs as veins crosscutting fluorite (Fig. 6h). The paragenetic sequence at the Bou Izourane deposit is summarized as follows: banded purple-white fluorite (F-2)-white fluorite (F-2)-calcite (Ca-2)-calcite (Ca3).

In the Tabeja deposit, the fluorite ore occurs in veins and vugs, but primarily in karstic cavities (up to 40 m^3). The latter cavities are frequently filled with purple fluorite and calcite minerals which cemented the Jurassic limestone angular blocks (Table 1, Figs. 5 and 9a-b). The interface between the ore and the host rock is sharp (Fig. 9a), indicating rapid brecciation likely caused by pressure fluctuations. Sometimes, fluorite forms euhedral, zoned purple crystals (Fig. 6i-j). The mineral paragenetic sequence is similar to that of the Bou Izourane deposit: banded purple-white fluorite (F-2)-calcite (Ca-2) (Fig. 9d-f). A few meters away from the orebodies, NE-SW- faults, N-S-trending faults, and N-S- to NNE-SSW-trending lamprophyre dikes are observed in the surroundings of the Tabeja deposit (Figs. 2 and 3).

6.2. Fluid and solid inclusions

Fluid and solid inclusions were investigated in samples of interstitial calcite (Ca-1) and fluorite (F-1) (IM13) hosted by altered aegirine-rich rock developed within the syenite at the Bou Imtessene deposit. The fluid inclusion study was also carried out in vein-type banded purple-white fluorite from the Tabeja deposit (TJ1) as well as banded purple-white fluorite (BZ1, BZ6, and BZ9) and white fluorite (BZ2, BZ3, and BZ5) from the Bou Izourane deposit (Figs. 10, 11, and 12). The microthermometric data from 103 fluid inclusions are shown in Fig. 13 and the Supplementary Data file. The identification of primary, pseudo-secondary, and secondary fluid inclusion assemblages (FIA's) followed the classic criteria described in Goldstein (2003), Goldstein and Reynolds (1994), and Roedder (1984).

6.2.1. Syenite-hosted Bou Imtessene deposit

The interstitial purple fluorite (F-1) from the Bou Imtessene deposit hosts secondary three-phase aqueous inclusions (L+V+S), which form trails that crosscut crystal boundaries (Fig. 10a). These fluid inclusions show regular shapes (cylindrical, cubic, spherical, prismatic, or negative crystal) and a small size (5-30 µm) (Fig. 10b). Petrographic observations show that they contain additional blurry-appearing solids (red arrows in Fig. 10b), which may be in disequilibrium with the inclusion fluid. The analyses of a solid phase (S) show two strong bands at 1071 $cm^{-1}$and 1090 cm^{-1} in the Raman spectrum, which indicate the

presence of shortite - $Na_2Ca_2(CO_3)_3$ - in the fluid inclusions (Fig. 11). The latter solid did not dissolve upon heating and only partial homogenization temperatures T_h(LVS→LS) were measured, which ranges between 163 to 213°C (median: 199°C). Pseudo-secondary/secondary fluid inclusions hosted in calcite from the same sample have shown similar T_h(LVS→LS) values of 194-197°C (median: 197°C). These fluid inclusions are small (8–10 µm), cubic in shape, and form trails terminating against crystal boundaries. The first melting temperatures (T_{fm}) of aqueous fluid inclusions hosted in both calcite and fluorite range between -50 and -46°C, indicating the presence of divalent cations in the solution (Bodnar, 2003). Fluorite-hosted inclusions show T_m(ice) values varying between -21 and -16.6°C (median: -18.3°C), corresponding to a salinity range of 19.9 to 23 wt. % NaCl equiv. (median: 21.2 wt.% NaCl equiv.). Calcite-hosted inclusions show relatively less variation in T_m(ice) values, ranging between -16.8 to -15.9°C (median: -16°C) and correspond to salinities of 19.4 to 20.1 wt. % NaCl equiv. (median: 19.4 wt. % NaCl equiv.). Due to similar T_h values and close salinity ranges, fluid inclusions in calcite, as well as fluorite, are considered Type 1 fluid inclusions.

The purple interstitial fluorite from IM13, IM14, and IM15 samples contain solid inclusions that caused the radiation-associated damage (Fig. 10c-d). The latter is manifested by halos surrounding the solids, their relics, or a cavity left behind by these solids (Fig. 10c-d). The halos' nuclei, the source of alpha radiation, are likely zircon and/or uraninite. In halo centers, the dark nuclei in places show hexagonal shapes (Fig. 10d), whereas the relict minerals may be spherical and yellowish in color (Fig. 10f) or exhibit elongated forms (Fig. 10c). The observed halos are multi-ring (Fig. 10e) or poorly developed, thus comprising only one outer ring (Fig. 10c-d).

6.2.2. Tabeja carbonate-hosted deposit

The banded purple-white fluorite (F-2) from the Tabeja deposit contains Type 2 primary two-phase (L+V±S) aqueous fluid inclusions of ca. 9-50µm in size, which display spherical, cylindrical or negative crystal shapes and are arranged parallel to growth and color zonation (Fig. 12a). Some of these inclusions contain an insoluble, tiny, prismatic solid that has not been identified. The inclusions homogenize to the

liquid phase at temperatures ranging between 118 and 157°C (median: 136°C), whereas the T_m(ice) values vary between -5.4 and -2.1°C corresponding to salinities of 3.5-8.4 wt.% NaCl equiv. (median: 5.9 wt.% NaCl equiv.).

6.2.3. Bou Izourane carbonate-hosted deposit

6.2.3.1. Banded purple-white fluorite

The banded purple-white fluorites (F-2) (samples BZ1, BZ9) contain Type 2 primary two-phase (L+V) aqueous inclusions (12-40 μm) showing a wide range of shapes from irregular to regular, i.e., spherical, cylindrical, cubic, and prismatic (Fig. 12b-c). They are decorating growth zones and are oriented perpendicularly to the color zonation (Fig. 12b). Beside primary inclusions, discrete trails of Type 3 aqueous two-phase (L+V) inclusions with lower L:V ratios are observed within the growth zones in samples BZ6 and BZ9 (Fig. 12c-d). The inclusion trails/planes terminate within the individual growth zones; therefore, they are likely pseudo-secondary. The inclusions within these trails/planes are microscopic (5-20 μm) and show regular shapes (predominantly spherical, cubic, and a negative crystal) (Fig. 12d), and locally they contain an additional optically distinguishable CO_2 phase (Fig. 12d inset).

Type 2 primary inclusions homogenized to the liquid phase at a temperature range of 124-137°C (median: 134°C), whereas the final melting temperature of ice varies between -4.1 and -0.9°C reflecting salinities of 1.6-6.6 wt.% NaCl equiv. (median: 5.1 wt.% NaCl equiv.). The first melting temperatures were observed in several of these inclusions, and their range between -27 and -42°C suggests that K^+, as well as Ca^{2+}/Mg^{2+} may be present in the aqueous solution (Bodnar, 2003). Homogenization temperatures of Type 3 pseudo-secondary inclusions vary depending on the FIA; however, they are consistent within an individual FIA's. In FIA1 the range is 218-261°C, median: 248°C, in FIA2: 303-317°C, median: 314°C, and in FIA3: 302-339°C, median: 335°C. The T_m(ice) values of these inclusions range overall between -1.8 and -0.3°C (median: -0.95°C) and correspond to salinities of 1.9-3.1 (FIA1), 0.5-1.4 (FIA2), and 0.7-0.8 (FIA3) wt.% NaCl equiv. (overall median: 1.7 wt.% NaCl equiv.).

6.2.3.2. White fluorite

The white fluorite (F-2) (samples BZ3, BZ5) hosts Type 2 primary two-phase (L+V) aqueous inclusions, which decorate growth zones. They are predominantly of elongated regular or irregular shapes and variable sizes (5-65 μm). Their T_h(LV→L) values of 130-155°C (median: 143°C) as well as T_m(ice) values (-5.5 to -2°C) are similar to values typical of Type 2 inclusions hosted in banded purple-white fluorites from Tabeja and Bou Izourane deposits. The salinities of Type 2 inclusions from white fluorites range between 3.4 and 8.5 wt.% NaCl equiv. (median: 6.0 wt.% NaCl equiv.). Besides non-boiling FIA's, the white fluorite (sample BZ2) also contains boiling (Fig. 12e) and flashing assemblages (Fig. 12f). The boiling FIA's consist of one-phase vapor (V) inclusions co-existing with two-phase (L+V) aqueous inclusions. The latter occur within darkened growth zones, and they are of very small sizes (1-3 μm); therefore, they could not be measured (Fig. 12e inset). The flashing FIA's also occur within growth zones, and they contain dark one-phase vapor (V) inclusions (Fig. 12f). The stretching, necking down, partial leakage textures or inconsistent liquid-to-vapor ratios were not observed in the vicinity of the boiling/flashing assemblages, which indicates these FIA's have not been affected by volumetric re-equilibration (Bodnar et al., 2003).

6.3. Carbon and oxygen isotopes

The C and O isotopic compositions of Jurassic carbonate, hydrothermally altered carbonate, skarn, carbonatite, and calcite samples are listed in Table 2 and Figure 14. The host Liassic limestones show $\delta^{18}O_{SMOW}$ values of 23.3-25.7‰ and $\delta^{13}C_{PDB}$ values of 0.8-2.3‰. These isotopic values fall within the range typical of marine Jurassic limestone (Hoefs, 2018; Land, 1980; Veizer and Hoefs 1976). The altered limestone samples display negative $\delta^{13}C_{VPDB}$ values (-3.7 to -2.5‰) and relatively lower $\delta^{18}O_{SMOW}$ values (20.6-21.8‰) than those of the unaltered limestones (Fig. 14). C and O isotopic signatures of skarns ($\delta^{13}C_{VPDB}$ = 0.4 to 1.7‰, $\delta^{18}O_{SMOW}$ = 25.3 to 26.0‰) resemble isotopic compositions of the unaltered Jurassic carbonates (Fig. 14). The C-O isotope data of carbonatites fall within or close to those reported for Tamazert carbonatites (Bouabdellah et al., 2010), Cape Verde and Canary Islands carbonatites (Hoernle et al., 2002; Hoernle and Tilton, 1991), and other carbonatites (Keller and Hoefs, 1995; Srivastava et al., 2022

and references therein) (Fig. 14). The $\delta^{13}C_{VPDB}$ and the $\delta^{18}O_{SMOW}$ values for syenite-hosted calcite (Ca-1) of the Bou Imtessene deposit range from -3.8 to -3.2‰, and from 9.9 to 10.2‰, respectively (Table 2, Fig. 14). The $\delta^{13}C_{VPDB}$ and $\delta^{18}O_{SMOW}$ values of Jurassic carbonate-hosted vein calcites (Ca-2) of the Bou Izourane and Tabeja deposits vary from -1.5 to 1.7‰, and from 10.4 to 15.2‰, respectively (Table 2, Fig. 14).

6.4. REY systematics

REY data of fluorite and calcite samples from the syenite-hosted ore deposit (Bou Imtessene) and the carbonate-hosted ore deposits (Tabeja and Bou Izourane), as well as the country rocks, are reported in Table 3. The chondrite-normalized REY patterns (REY_{CN}) of these mineral and rock samples are shown in Figure 15. The REY are normalized to C1 chondrite (Barrat et al., 2012) (Fig. 14). The averaged total REY concentrations in fluorite (∑REY= 1552 ppm) and calcite (∑REY= 119 ppm) of the syenite-hosted ore deposit (Bou Imtessene) are higher than those from the carbonate-hosted deposits of Tabeja (fluorite: ∑REY= 9.60 ppm, calcite: ∑REY = 26.09 ppm) and Bou Izourane (fluorite ∑REY= 17.38 ppm, calcite: ∑REY = 18.53 ppm). Overall, the analyzed country rocks that crop out in the mining area display relatively low average total REY concentrations in the range of 3.13 ppm (limestone) to 590 ppm (carbonatite) (Table 4). In the syenite-hosted ore deposit, fluorite, calcite, and the igneous rocks (syenite, lamprophyre, and carbonatite) display strikingly similar chondrite-normalized patterns with a certain light rare earth elements (LREY) enrichment in chondrite-normalized patterns (Fig. 15). In the carbonate-related deposits, fluorite, calcite, limestone, and the hydrothermally altered marl samples show similar chondrite-normalized patterns with generally more flat patterns and a relatively less $LREY_{CN}$ enrichment. The Jurassic limestone shows negative Ce_{CN} anomalies and positive La_{CN}, Gd_{CN}, and Y_{CN} anomalies (Fig. 15), whereas the marl has two orders of magnitude higher concentrations of REY with a small negative Ce_{CN} anomaly and a positive Y_{CN} anomaly. The yttrium anomaly is positive for all studied fluorite and calcite samples ($Y/Y^* >> 1$) (Table 3).

7. Discussion

7.1. Evolution of the ore-forming fluids

The fluid inclusion study reveals that fluids of different origins (Fig. 13) were mobilized within one large, long-lived hydrothermal system centered around the Tamazert alkaline igneous complex. Different types of fluid inclusions were observed in fluorite and calcite from syenites and adjacent carbonate-hosted deposits (Fig. 13), and they reflect different hydrological conditions (Sośnicka et al., 2021). Pressure corrections are minimal due to the emplacement of syenite at shallow depths (< 3km, Salvi et al., 2000). Hence, the homogenization temperatures of fluid inclusions hosted in interstitial minerals in the altered syenite can be used as a proxy for the true trapping temperatures.

7.1.1. Fluid migration in syenite

The high salinity (19.4 to 23 wt.% NaCl equiv.) secondary Type 1 fluid inclusions (stage 1) represent a magmatic-hydrothermal fluid. The blurry interior appearance of some of these inclusions suggests that the solid, identified as shortite (Fig. 10b), may be in disequilibrium with the inclusion fluid. Thus, it was likely formed by the reaction of the inclusion liquid and the fluorite host. Sparse experimental studies show that shortite crystallizes at T=125-300°C and 2 kbar, reaching equilibrium at 90±25°C (Bradley and Eugster, 1969). Therefore, the T_h values (163-213°C) and petrographic observations suggest that shortite has not reached equilibrium with the liquid phase in Type 1 fluid inclusions. Shortite has been previously recognized in natrocarbonatites as an exotic subsolidus mineral and a low-temperature alteration product (Zaitsev et al., 2008). The presence of shortite is evidence for migration of the residual magmatic-hydrothermal fluids, which exsolved from the nepheline syenite or carbonatites at late stages of magmatic activity. Alternatively, this exotic mineral (i.e., shortite) could be derived from the dissolution of the Jurassic carbonates and the subsequent infiltration of calcium at a depth where Ca metasomatism of syenites could occur. The lack of Eu anomalies in REY_{CN} patterns of the ore minerals (Fig. 15b-c) indicates that the

temperatures of Na-Ca-metasomatizing fluids have not reached 250°C; therefore, the Type 1 secondary fluid inclusions were entrapped shortly after precipitation of the interstitial fluorite and calcite.

The magmatic-hydrothermal origin of interstitial fluorites is supported by the presence of solid inclusions with halos manifesting radiation-induced damage to the host (Fig. 10c-f). The damage is attributed to radionuclides in the ^{238}U decay chain (Dill and Weber, 2010). Many halos in purple interstitial fluorites developed a complete set of rings displaying the full spectrum of α-particle emitting radionuclides (Fig. 10e). However, there are also halos with one ring only, which are poorly developed polonium halos ascribed to radionuclides succession: ^{225}Ra, ^{210}Po, ^{222}Rn, ^{218}Po, and ^{214}Po (Dill and Weber, 2010). The nepheline syenites of the Tamazert complex are enriched in zirconium (Salvi et al., 2000); therefore, U-rich and Zr-rich mineral phases appear to be the most likely sources of alpha radiation, which caused fluorite damage. These halo-inducing radioactive inclusions could also be attributed to uraninites. Similar radiogenic uraninite inclusions were observed in the purple fluorite of the La Azul epithermal fluorite ore deposit in southern Mexico (Pi et al., 2007). The hexagonally as well as spherically shaped dark nuclei (Fig. 10d-e) could be likely after zircon and/or uraninite, whereas the elongated phases are likely to be baddeleyite (Fig. 10c). The signatures from these radioactive minerals may contribute to the "U-shaped" REY patterns of highly fractionated nepheline syenites, as their presence results in depletion of HREE's relative to LREE's (Fig. 15a) (Rollinson, 1993). The well-developed halos, which show full ring sets, are syngenetic to fluorite and indicate that U was carried by the F-rich fluid as fluorocomplexes (Aiuppa et al., 2009). The polonium halos may be attributed to an early alteration event (Dill and Weber, 2010) that could be related to the migration of Na-Ca metasomatizing fluids represented by Type 1 fluid inclusions.

Another line of evidence supporting the magmatic-hydrothermal origin of interstitial fluorites and calcites in nepheline syenites is the REY inventory of these minerals. The REY_{CN} patterns and high ∑REY values of both interstitial minerals are similar to REY trends of the Tamazert igneous rocks: syenites, lamprophyres, and carbonatites (Fig. 15a-c). This leads to the conclusion that the REY inventory of interstitial fluorites and calcites at the Bou Imtessene deposit has been derived from the magmatic-hydrothermal source.

The $\delta^{13}C$ and $\delta^{18}O$ isotopic values of syenite-hosted interstitial calcite (Ca-1) from Bou Imtessene plot close to the range of isotopic values typical for the igneous rocks ($\delta^{13}C_{VPDB}$ = −10 to −5‰, Ohmoto and Goldhaber, 1997; $\delta^{18}O_{SMOW}$ ~ -5 to 12‰, Hoefs, 2009, 2018). The oxygen isotopic compositions of these calcites are also similar to O isotopic signatures of carbonatites located NW of Bou Imtessene (Table 2). It is commonly accepted that the residual fluids exsolving from peralkaline melts are highly enriched in fluorite and depleted in Ca (Webster, 1990). Consequently, calcium in Type 1 brine inclusions could have originated from interaction with external fluids or a carbonatitic source. Based on the above-mentioned considerations, the Type 1 fluid inclusions represent a late-stage, modified high salinity alteration fluid of primarily magmatic-hydrothermal origin, that migrated shortly after the precipitation of magmatic-hydrothermal fluorite at T<250°C.

7.1.2. Fluid circulation in Jurassic carbonates

Jurassic carbonate-hosted fluorite from both Tabeja and Bou Izourane deposits precipitated from overall low salinity fluids (1.6-8.5 wt.% NaCl equiv.) at a temperature range of 118-157°C as evidenced by Type 2 primary inclusions (Fig. 13). These salinities and temperatures are significantly lower compared to data from the interstitial fluorites hosted in altered syenites. Low salinities and temperatures indicate that the fluids responsible for the precipitation of carbonate-hosted fluorites are of meteoric origin. The non-magmatic origin of the ore-forming fluids is also supported by REY data of carbonate-hosted fluorites and calcites from Tabeja and Bou Izourane deposits (Fig. 15b-c). The REY patterns of fluorites and calcites do not show considerable Eu_{CN} anomalies and are similar to those of the carbonate host rocks (Fig. 15a-c), which suggests that they inherited their REY inventory from (possibly Liassic) carbonate rocks. Based on these considerations, the most likely mechanisms leading to purple-white fluorite precipitation are cooling and fluid-wall rock interaction.

The presence of Type 3 fluid inclusions in banded purple-white fluorites from the Bou Izourane deposit indicates that fluorite precipitation from the meteoric fluids was interrupted by the intermittent influx of high temperature (218-339°C) and low salinity (0.5-3.1 wt.% NaCl equiv.) fluids (Fig. 13). Very

low salinities point towards the meteoric origin of the latter fluids, however they are relatively lower compared to the ore-forming fluid (Fig. 13). Temperature variations among different Type 3 FIA's were caused by heating up at depths to different degrees due to fluid convection induced by elevated geothermal gradients developed around relatively shallow Tamazert igneous intrusion. The vanishing magmatic activity provided the heat necessary to drive the large-scale fluid circulation. Alternatively, the magmatic-hydrothermal origin of the high-temperature Type 3 fluids cannot be excluded. The presence of carbon dioxide in the high-temperature Type 3 fluid inclusions (Fig. 12d inset) may suggest a minor magmatic contribution or derivation of CO_2 from the dissolution of Jurassic carbonates during interaction with the high-temperature (218-339°C) fluid. However, CO_2-rich magmatic gas phase could have dissolved into downdrawn heated meteoric fluids, simultaneously causing a relative salinity decrease of the meteoric fluid. This would increase fluid acidity and cause more efficient fluorine scavenging from the surrounding F-rich igneous rocks. Other possibilities are that the high-temperature Type 3 fluids represent fluids sourced from the lamprophyre dikes. These fluids could have been released episodically into the hydrological system during the precipitation of banded purple-white fluorite from meteoric fluids. These scenarios, including magmatic-hydrothermal contribution, are not unlikely since the Bou Izourane ore deposit is controlled by a deep-seated fault zone (Fig. 5), which is a perfect conduit facilitating fluid transfer to shallower crustal levels. In the Tabeja deposit, Type 3 fluid inclusions were not observed, likely due to a lack of connection to major deep-seated structures.

The carbonate-hosted white fluorite from the Bou Izourane deposit contains alternating growth zones with non-boiling, boiling, and flashing FIA's, which indicate a dynamically evolving hydrothermal system at shallow levels (Fig. 12e-f). These fluid inclusion data evidence the evolution of P-T conditions as well as ore-forming mechanisms during the precipitation of white fluorite. A change from non-boiling conditions to boiling and flashing conditions indicates significant fluid pressure fluctuations in the hydrothermal system (Moncada et al., 2012). The rapid and significant pressure drop from near-lithostatic to below hydrostatic during rock fracturing may lead to instantaneous vaporization of the fluid ("flashing")

(Moncada et al., 2012). The extensive breccia zones encountered in both Bou Izourane and Tabeja deposits (Figs. 8b-c and 9a-b) also suggest rapid pressure fluctuations and intense fluid-wall rock interactions.

The $\delta^{13}C$ and $\delta^{18}O$ values of the Jurassic carbonate-hosted vein calcites (Ca-2) plot in the area between the fields of Jurassic limestones and igneous rocks (Fig. 14). Such intermediate isotopic signatures may be produced by fluid-wall rock interactions (Taylor, 1997) or mixing of fluids from different sources. Using the equilibrium fractionation equation of O'Neil et al. (1969), median temperatures of 133 and 135°C, measured in calcite from the Bou Izourane deposit (samples BZ1 and BZ9), and measured $\delta^{18}O_{SMOW}$ values (12.8-15.2‰) in the same calcite samples (Table 2), the calculated $\delta^{18}O_{SMOW}$ values of the aqueous fluid are -1.0 and +1.2‰. These values confirm that the fluid responsible for the precipitation of vein calcite accompanying fluorite was primarily meteoric water (N'da et al., 2016).

7.2. REY constraints on fluid chemistry and transport

Overall, the REY concentrations of syenite-hosted fluorite (F-1) and calcite (Ca-1) are higher than those of Jurassic carbonate-hosted fluorite (F-2) and calcite (Ca-2), especially with regard to the lighter REY (Table 3, Fig. 15). Higher REY contents in fluorite associated to carbonatite—alkaline igneous rocks compared to those for fluorite in carbonate-hosted ore were also observed for the Late Cretaceous to Miocene ore deposits in Turkey (Öztürk et al., 2019). The strikingly similar chondrite-normalized REY patterns of the Tamazert igneous rocks (syenite, carbonatite, and lamprophyre) and the interstitial minerals (i.e., F-1 and Ca-1) at Bou Imtessene support a magmatic-hydrothermal origin of the fluids that are involved in the precipitation of the syenite-related mineralization. The syenite-hosted fluorite and calcite also do not show a strong Eu_{CN} anomaly, indicating that the magmatic-hydrothermal ore-forming fluids did not reach 200-250°C prior to mineral precipitation. At temperatures usually in excess of ca 250°C, Eu(III) is reduced to Eu(II) and can thus be decoupled from its strictly trivalent REY neighbors (Bau, 1991; Möller et al., 1994; Sverjensky, 1984). Especially fluorite is known to show positive Eu anomalies in normalized patterns if the fluid temperatures exceeded 200-250°C prior to the mineral formation (i.e., in the Pennine Orefield,

UK: Bau et al., 2003; Kraemer et al., 2019). Hence, low temperatures (<200-250°C) that prevailed in the hydrothermal system, as indicated by Eu geothermometry, are in agreement with microthermometric data.

The vein fluorite (F-2) and calcite (Ca-2) from the carbonate-hosted ore deposits show overall similar REY_{CN} patterns to those of the Jurassic marls and limestones (Fig. 15a-b), indicating water-rock interaction and REY leaching from these formations by the heated meteoric fluid. The lack of a strong Eu anomaly in the carbonate-hosted fluorite and calcite suggests low fluid temperatures prior to mineral precipitation (<250°C). This conclusion is corroborated by the fluid inclusion data of the carbonate-hosted fluorite, which revealed low temperature (118-157°C) and low salinity (1.6-8.4 wt. % NaCl equiv.) fluids, typical of heated meteoric waters.

Owing to the abundance of calcite, particularly in the Jurassic carbonate-hosted ore deposits, and due to the presence of fluorite, REY-carbonato and -fluoro complexes have played a significant role in REY transport and/or deposition. The enrichment of Y (i.e., Y_{CN} anomaly) in fluorites (Y/Y* = 1.67- 2.17) and calcites (Y/Y* = 1.32-1.34) is related to the significantly higher stability constants of Y-fluorocomplexes relative to Ho-fluorocomplexes (Bau, 1996; Bau and Dulski, 1995). However, it is emphasized that the Y anomaly may also have been inherited from the hydrothermal fluid or the surrounding country rocks, as all of them, including the magmatic suite, show minor positive Y_{CN} anomalies in their bulk rock compositions (Fig. 15). Salvi et al. (2000) had already suggested fluorocomplexes as carriers for HFSE and REY transportation in the Tamazert magmatic-hydrothermal system. We conclude that Cl^-, F^- and CO_3^{2-} and/or HCO_3^- complexes were responsible for the mobilization and transport of REY in the hydrothermal fluid. The destabilization of these complexes, particularly of the F^- complexing agents, through e.g., fluid-wall rock interaction, led to fluorite precipitation.

7.3. Constraints on sources of fluorine and REY

According to recent studies (e.g., Bouabdellah et al., 2010; Kchit, 1990; Marks et al., 2009), the igneous rocks of the Tamazert complex originated from fractional crystallization of the mantle-derived magma, which was affected by crustal assimilation, and thus interaction with surrounding sediments, namely Jurassic carbonates. These considerations alone primarily point toward a mantle source of fluorine-rich melts. During magma differentiation in a closed system, fluorine partitions into the residual silicate melt if F^- concentrations in the melt are below ca. 7-8 wt. % (Webster, 1990). Progressive crystallization of minerals such as micas, apatite, fluorite, or amphiboles leads to a decrease of F^- concentrations in the remaining residual melt (Aiuppa et al., 2009; Gabitov et al., 2005). Recent studies have shown that minerals forming the Tamazert syenite have elevated fluorine contents, i.e., average concentrations of fluorine in apatite, biotite, amphibole, and titanite are 3.2%, 2.6 %, 1.1%, and 0.6%, respectively, whereas the estimated F^- content in the melt ranges between 1500 ppm and 2500 ppm (Wang et al., 2014). Such low fluorine concentrations may suggest that the interstitial fluorite (F-1) precipitated directly from a residual melt. However, owing to the low crystallization temperatures (<250°C), based on REY inventory, it is unlikely that it formed directly from a high-temperature melt. Significant amounts of fluorine may partition into the late-stage aqueous magmatic-hydrothermal fluids from alkaline/carbonatite melts and may lead to the metasomatism of the silicate rocks (e.g., Dolejš and Baker, 2007; Mangler et al., 2014; Webster, 1990). The secondary fluid inclusion (Type 1) trails most likely represent a late Na-Ca metasomatic fluid, which altered syenites and migrated after fluorite (F-1) crystallization. In shallowly emplaced systems that are susceptible to fluid loss through e.g., surrounding fault systems, degassing of F-bearing species may also occur during fractional crystallization (Aiuppa et al., 2009). Since the shallow Tamazert intrusion is centered on an interconnected fault network, such degassing might have episodically occurred and is likely recorded by fluorite (F-2)-hosted high-temperature Type 3 secondary fluid inclusions (T_h=218-339°C).

The Jurassic carbonate-hosted ores show a lower degree of fractionation of LREY relative to MREY and HREY than the syenite-hosted ores, which show steeper patterns that closely resemble the igneous suite. Pristine marine limestones, formed in an oxygenated environment, usually display negative

Ce anomalies in normalized patterns, a signal that is inherited from seawater, where Ce(III) is oxidatively scavenged as Ce(IV) from the water column by oxyhydroxide minerals (i.e., Bau and Koschinsky, 2009), leaving behind Ce-depleted seawater. Both the pristine limestone and the marl show small negative Ce_{CN} anomalies in addition to further signatures indicative of formation from such seawater, i.e., positive La_{CN} and Y_{CN} anomalies (Tostevin et al., 2016) (Fig. 15a). The pristine limestone also displays a typical positive Gd_{CN} anomaly. Carbonate-hosted fluorites and calcites show, to different extents, a variety of these 'limestone' features in their REY_{CN} patterns. The carbonate-hosted fluorites from Bou Izourane deposit display all four features (positive La_{CN}, Gd_{CN}, Y_{CN}, and negative Ce_{CN} anomalies), whereas the carbonate-hosted fluorites and calcites from Tabeja deposit and the carbonate-hosted calcites from Bou Izourane deposit show at least two of these features (Fig. 15). In addition to these observations, the high similarity to the patterns of the limestone host units (Fig. 15) also argues in favor of the fact that REY in the carbonate-hosted ores were sourced from Jurassic limestones and not from the igneous suite of rocks.

8. Conclusions

Based on geological observations, mineralogical, geochemical and stable isotopic constraints, different major types of ore-related fluid systems, as well as the mechanisms of fluorite ore precipitation, were identified and are summarized as follows:

1) The REY-enriched interstitial fluorite (F-1), hosted in aegirine-rich syenite, precipitated from a F-rich magmatic-hydrothermal fluid, which exsolved from the highly evolved alkaline-silicate melt and rapidly cooled to temperatures below 250°C. This event was subsequently followed by migration of post-fluorite (F-1) Na-Ca metasomatic brines of unclear origin but likely related to later carbonatitic or lamprophyre intrusions. Partitioning of F^- into the magmatic fluid phase was facilitated by magma ascent to the shallow crustal levels in response to the reactivation of the NE-SW-trending fault system.
2) Banded fluorite (F-2) deposits hosted in Jurassic carbonates, located in the vicinity of the Tamazert igneous complex, precipitated from low temperature (118-157°C) and low salinity fluids (1.6-8.5

wt.% NaCl equiv.) of primarily meteoric origin. The circulation of these fluids was driven by the heat flow around the shallow intrusive body and the possible influence of emanations of hot magmatic gases/fluids from syenite or later carbonatite/lamprophyre intrusions into the hydrological system. The inferred deposition mechanisms include cooling, fluid-wall rock interactions, and pressure fluctuations. Karstic features and deep-seated structural discontinuities have facilitated fluid transport.

3) Fluorine and REY in syenite-hosted fluorites were sourced from the evolving alkaline-silicate melt, whereas heated meteoric fluids precipitating carbonate-hosted fluorite veins acquired fluorine by leaching the syenites and presumably other F-rich igneous rocks. In contrast, the REY inventory of the latter fluorite veins has been acquired by fluid interaction with Jurassic carbonates.
4) The Cl^-, F^- and CO_3^{2-} and/or HCO_3^- complexes were responsible for the mobilization and transport of REY in hydrothermal fluids. The destabilization of F^- complexing agent by e.g., fluid-wall rock interactions led to the precipitation of fluorite ores.

This study reveals the importance of processes such as differentiation of the mantle-derived alkaline-silicate F-rich magmas, alteration, fluid cooling, fluid-wall rock interactions, and decompression at shallow crustal levels in the formation of abundant fluorite deposits centered in and around the Tamazert alkaline igneous complex. Future studies of these fluorite deposits should focus on constraining Ca sources and determining the accurate ages of mineralization of various ore types. This would allow a better understanding of the genetic relationships between igneous rocks and fluorite deposits.

Acknowledgement

The first author would like to thank the Professional Staff Congress of the City University of New York (PSC/CUNY) for funding this project. We are grateful to Dr. Giles Levresse, Dr. Fernando Tornos, and the anonymous reviewers for their insightful comments and suggestions that improved the quality of this paper.

We are also grateful to the Associate Editor and the Editor-in-Chief, Dr. Read Brown Mthanganyika Mapeo, for their comments and handling of this paper.

References

Achmani, J., 2017. Etude des minéralisations Fluorées de la région de Bou-Izourane (Haut Atlas Oriental, Maroc). Unpublished Maters, Faculté des Sciences, Casablanca, 61p.

Agard, J., 1973. Carte géologique du complexe de roches alcalines à carbonatites de Tamazeght (Haut Atlas de Midelt, Maroc). Notes et Mémoires du Service Géologique du Maroc 248.

Agard, J., 1977. Notice explicative de la carte géologique du complexe de roches alcalines à carbonatites du Tamazeght (Haut Atlas de Midelt, Maroc). C. R. d'Activité Annuelle. Rabat: Direction de Géologie Rabat.

Aiuppa, A., Baker, D.R., Webster, J.D., 2009. Halogens in volcanic systems. Chem. Geol. Halogens in volcanic systems and their environmental impacts 263, 1–18. https://doi.org/10.1016/j.chemgeo.2008.10.005.

Al-Haderi, M., Tayebi, M., Bouabdli, A. El-Hanbali, M., 1998. Chronologie et conditions de mise en place des différents faciés pétrographiques du complexe alcalin de Tamazert (Haut Atlas de Midelt, Maroc). Afr. Geosci. Rev. 5, 159-171.

Alvin, M.P., Dunphy, J.M., Groves, D.I., 2004. Nature and genesis of a carbonatite-associated fluorite deposit at Speewah, East Kimberley Region, Western Australia. Mineral. Petrol. 80,127-153.

Barrat, J.A., Zanda, B., Moynier, F., Bollinger, C., Liorzou, C., Bayon, G., 2012. Geochemistry of CI chondrites: Major and trace elements, and Cu and Zn isotopes. Geochim. Cosmochim. Acta 83, 79-92.

Bau, M., 1991. Rare-earth element mobility during hydrothermal and metamorphic fluid rock interaction and the significance of the oxidation state of europium. Chem. Geol. 93, 219–230. https://doi.org/10.1016/0009-2541(91)90115-8.

Bau, M., 1996. Controls on the fractionation of isovalent trace elements in magmatic and aqueous systems: Evidence from Y/Ho, Zr/Hf, and lanthanide tetrad effect. Contrib. Mineral. Petrol 123(3):323 - 333. https://doi.org/10.1007/s004100050159.

Bau, M., Dulski, P., 1995. Comparative study of yttrium and rare-earth element behaviours in fluorine-rich hydrothermal fluids. Contrib. Mineral. Petrol. 119 (2–3), 213–223. https://doi.org/10.1007/BF00307282.

Bau, M., Dulski, P., 1999. Comparing yttrium and rare earths in hydrothermal fluids from the Mid-Atlantic Ridge: implications for Y and REE behaviour during near-vent mixing and for the Y/Ho ratio of Proterozoic seawater. Chem. Geol. 155, 77–90.

Bau, M., Romer, R.L., Lüders, V., Dulski, P., 2003. Tracing element sources of hydrothermal mineral deposits: REE and Y distribution and Sr-Nd-Pb isotopes in fluorite from MVT deposits in the Pennine Orefield, England. Miner. Deposita 38, 992–1008 https://doi.org/10.1007/s00126-003-0376-x.

Bau, M., Koschinsky, A., 2009. Oxidative scavenging of cerium on hydrous Fe oxide: Evidence from the distribution of rare earth elements and yttrium between Fe oxides and Mn oxides in hydrogenetic ferromanganese crusts. Geochem. J. 43,37-47.

Bodnar, R.J., 2003. Reequilibration of fluid inclusions. In Samson, I., Anderson, A., Marshall, D. (Eds.), Fluid Inclusions: Analysis and Interpretation. Mineral. Assoc. Canada Short Course, v. 32, pp. 213–230.

Bouabdli, A., Dupuy, C., Dostal, J., 1988. Geochemistry of Mesozoic Alkaline Lamprophyres and related Rocks from the Tamazert Massif, High Atlas (Morocco). Lithos. 22(1), 43–58.

Bouabdellah, M., Hoernle, K., Kchit A., Duggen S., Hauff, F., Klügel, A., Beaudoin, G., 2010. Petrogenesis of the Eocene Tamazert continental carbonatites (Central High Atlas, Morocco): Implications for a common source for the Tamazert and Canary and Cape Verde Island carbonatites. J. Petrol. 51(8), 1655–1686.

Bouabdellah, M., Sangster, D., 2016. Geology, geochemistry, and current genetic models for major Mississippi Valley-Type Pb–Zn Deposits of Morocco. In: Bouabdellah, M., Slack, J.F. (Eds.), Mineral Deposits of North Africa: Cham. Springer International Publishing, Switzerland, pp. 463–495. https://doi.org/10.1007/978-3-319-31733.

Bouabdellah, M., Zemri, O., Jébrak, M., Klügel, A., Levresse, G., Maacha, L., Gaouzi, A., Souiah., M., 2016. Geology and Mineralogy of the El Hammam REE-Rich Fluorite Deposit (Central Morocco): A Product of Transtensional Pangean Rifting and Central Atlantic Opening. In Mineral Deposits of North Africa, Mineral Resource Reviews; Bouabdellah, M., Slack, J.F., Eds.; Springer: Cham, Switzerland, pp. 307–324.

Bouhlel, S., Fortune, J.P., Guilhaumou, N., Touray, J.C., 1988. Les minéralisations stratiformes á F-Ba de Hammam Zriba-Jebel Guebli (Tunisie nord-orientale): l'apport des études d'inclusions fuides á la modélisation génétique. Miner. Deposita 23, 166–173.

Bradley, W.H., Eugster, H.P., 1969. Geochemistry and paleolimnology of the trona deposits and associated authigenic minerals of the Green River Formation of Wyoming. US Geol. Surv. Professional Paper, 496-B, 71 pp.

Buhn, B., Rankin, A.H., Schneider, J., Dulski, P., 2002. The nature of orthomagmatic, carbonatitic fluids precipitating REE, Sr-Rich fluorite, fluid-inclusion evidence from the Okorusu fluorite deposit, Namibia. Chem. Geol. 186, 75-98.

Charrière, A., Haddoumi, H., 2016. Les Couches rouges continentales Jurassico-Crétacées des Atlas Marocains (Moyen Atlas, Haut Atlas central et oriental): Bilan stratigraphique, paléogéographies successives et cadre géodynamique. Boletin Geologico y Minero 127 (2/3), 407–430 (in French).

Deng, X.H., Chen, Y.J., Bagas, L., Zhou, H.Y., Yao, J.M., Zheng, Z., Wang, P., 2015. Isotope (S–Sr–Nd–Pb) constraints on the genesis of the ca. 850Ma Tumen Mo–F deposit in the Qinling Orogen, China Precambr. Res. 266, 108-118.

Duggen, S., Hoernle, K., Hauff, F., Klügel, A., Bouabdellah, M., Hirlwall, M.F., 2009. Flow of Canary mantle plume material through a subcontinental lithospheric corridor beneath Africa to the Mediterranean. Geol. 37, 283-286.

Dulski, P., 2001. Reference materials for geochemical studies: New analytical data by ICP-MS and critical discussion of reference values. Geostandards Newsletter: J. Geostand. Geoanal., 25, 87-125.

Dill, H.G., Weber, B., 2010. Accessory minerals of fluorite and their implication concerning the environment of formation (Nabburg-Wölsendorf fluorite district SE Germany)—with special reference to fetid fluorite ("Stinkspat"). Ore Geol. Rev. 37, 65–86.

Dolejš, D., Baker, D.R., 2007. Liquidus equilibria in the system K_2O-Na_2O-Al_2O_3-SiO_2-F_2O_{-1}-H_2O to 100 MPa: II. Differentiation paths of fluorosilicic magmas in hydrous systems. J. Petrol. 48, 807–828. https://doi.org/10.1093/petrology/egm002.

Du Dresnay, R., 1979. Sédiments jurassiques du domaine des chaînes atlasiques du Maroc. Symp. "Sédimentation jurassique W-européen" Paris, 1977. Publ. Spéc. Assoc. Sedim. Fr. 1, 345–355.

Du Dresnay, R., 1987. Jurassic development of the region of the Atlas Mountains of Morocco chronology, sedimentation, and structural significance. In: Cornelius, C.D., Jarnas, M., Lehmann, E.P. (Eds.), Geology and Culture of Morocco. Earth Sci. Soc Libya, Eighteenth Field Conference, pp. 77–99.

Ellero, A., Malusà, M.G., Ottria, G., Ouanaimi, H., Froitzheim, N., 2020. Transpressional structuring of the high atlas belt, Morocco. J. Struct. Geol. 135, 104021. https://doi.org/10.1016/j.jsg.2020.104021.

Ellouz, N., Patriat, M., Gaulier, J.M., Bouatmani, R., Sabounji, S., 2003. From rifting to Alpine inversion: Mesozoic and Cenozoic subsidence history of some Moroccan basins. Sediment. Geol. 156, 185–212.

El Ouali, M., Kabiri, L., Essafraoui, B., Charroud, A., Krencker, F.N., Bodin, S., 2021. Stratigraphic and geodynamic characterization of Jurassic–Cretaceous "red beds" on the Msemrir–Errachidia E–W transect (central High Atlas, Morocco). J. Afri. Earth Sci. 183,104330. https://doi.org/10.1016/j.jafrearsci.2021.104330.

Emberger, A., 1965. Eléments pour une synthèse métallogénique du district plombifère de la Haute Moulouya. In: Colloque sur des gisements stratiformes de Plomb, Zinc et Manganèse du Maroc 1962. Notes Mém. Serv. Géol. Maroc 181, 235–238.

Essaifi, A., Zayane, R., 2018. Petrogenesis and origin of the upper Jurassic-lower Cretaceous magmatism in central high atlas (Morocco): major, trace element and isotopic (Sr-Nd) constraints. J. Afr. Earth Sci. 137, 229–245. https://doi.org/10.1016/j.jafrearsci.2017.10.002.

Frizon de Lamotte, D., Leturmy, P., Missenard, Y., Khomsi, S., Ruiz, G., Saddiqi, O., Guillocheau, F., Michard, A., 2009. Mesozoic and Cenozoic vertical movements in the Atlas system (Algeria, Morocco, Tunisia): an overview. Tectonophysics 475, 9–28.

Ohmoto, H., Goldhaber, M.B., 1997. Sulfur and carbon isotopes H.L. Barnes (Ed.), Geochemistry of Hydrothermal Ore Deposits (third ed.), Wiley, New York, pp. 517-611.

O'Neil, J.R., Clayton, R.N., Mayeda, T.K., 1969. Oxygen isotope fractionation in divalent metal carbonates. J. Chem. Phy. 51, 5547–5558.

Ouanaimi, H., Soulaimani, A., Baidder. L., Eddebbi, A., Hoepffner, C., 2018. Unraveling a distal segment of the west African craton Paleozoic margin: Stratigraphy of the Mougueur inlier of the eastern High Atlas, Morocco. Compt. Rendus Geosci. 350, 289–298. https://doi.org/10.1016/j.crte.2018.06.008.

Ovtracht, A., 1978. Province plombo-zincifère du Haut-Atlas central. Mines. Géol. Energ. Rabat. Maroc. 44, 103–109 (in French).

Gabitov, R.I., Price, J.D., Watson, E.B., 2005. Solubility of fluorite in haplogranitic melt of variable alkalis and alumina content at 800°–1000°C and 100 MPa. Geochem. Geophys. 6, https://doi.org/10.1029/2004GC000870.

Goldstein, R.H., 2003. Petrographic analysis of fluid inclusions. Mineralogical Association of Canada, Short Course 32, p. 9–53.

Goldstein, R.H., Reynolds, T.J., 1994. Systematics of fluid inclusions in diagenetic minerals. Society for Sedimentary Geology, Short Course 31, 199 p.

González-Partida, E., Carrillo, C.A., Grimmer, J.O.W., Pironon, J., Mutterer, J., Levresse, G., 2003. Fluorite Deposits at Encantada-Buenavista, Mexico, Products of Mississippi Valley Type Process. Ore Geol, Rev. 23, 107-124.

Hoefs, J., 2009. Stable Isotope Geochemistry, sixth ed., Springer-Verlag. doi: 10.1007/ 978-3-540-70708-0.

Hoefs, J., 2018. Isotope Fractionation Processes of Selected Elements. In: Stable Isotope Geochemistry. Springer Textbooks in Earth Sciences, Geography and Environment. Springer, Cham. https://doi.org/10.1007/978-3-319-78527-1_2.

Hoernle, K., Tilton, G., 1991. Sr-Nd-Pb isotope data for Fuerteventura (Canary Islands) basal complex and subaerial volcanics: applications to magma genesis and evolution. Schweizerische Mineralogische und Petrographische Mitteilungen 71, 5-21.

Hoernle, K., Tilton, G., Le Bas, M.J., Duggen, S., Garbe Schönberg, D., 2002. Geochemistry of oceanic carbonatites com- pared with continental carbonatites: mantle recycling of oceanic crustal carbonate. Contrib. Mineral. Petrol. 142, 520–542.

Hill, G.T., Campbell, A.R, Kyle, P.R., 2000. Geochemistry of southern New Mexico fluorite occurrences implications for precious metals exploration in fluorite-bearing systems. J. Geochem. Explor. 68, 1–20.

Jemmali, N., Rddad, L., Souissi, F., Carranza, E.J., 2019. The ore genesis of the Jebel Mecella and Sidi Taya F Ba (Zn Pb) Mississippi Valley-type deposits, Fluorite Zaghouan Province, NE Tunisia, in relation to Alpine orogeny: Constraints from geological, sulfur, and lead isotope studies. C. R. Geosci. 351, 312-320.

Jenny, J., Le Marrec, A., Monbaron, M. 1981. Les couches rouges du Jurassique moyen du Haut Atlas central (Maroc). Corrélations lithostratigraphiques, éléments de datation et cadre tectono-sédimentaire. Bull. Soc. Geol. Fr. 23 6 (7), 627–639 (in French).

Karaoui, A., Breitkreuz, C., Karaoui, B., Yajioui, Z., Mahmoudi, A., 2022. Facies architecture, modal analysis and geochemistry of the Early Ediacaran turbiditic series in the Skoura inlier (Central High Atlas,

Morocco): Implications for provenance and geotectonic setting. J. Afric. Earth Sci.185, 104390. https://doi.org/10.1016/j.jafrearsci.2021.104390.

Kchit, A., 1990. Le complexe plutonique alcalin du Tamazert, Haut Atlas de Midelt (Maroc). Pétrologie et structurologie. PhD thesis, Université de Toulouse, 302 p.

Keller, J., Hoefs, J., 1995. Stable isotope characteristics of recent natrocarbonatites from Oldoinyo Lengai. In: Bell, K. and Keller, J. (Eds) Carbonatite Volcanism: Oldoinyo Lengai and the Petrogenesis of Natrocarbonatites. IAVCEI Proc Volcanol 4. Berlin, Springer, pp. 113–123.

Klein, J.L., Harmand, C., 1985. Le volcanisme de la région Zebzate: âge et relations avec le complexe alcalin à carbonatites du Tamazert (Haut Atlas de Midelt, Maroc). In: 110ème Congrés National des Sociétés Savantes. Montpellier Sci. Fascicule VI, 147-152.

Kraemer, D., Viehmann, S., Banks, D., Sumoondur, A.D., Koeberl, C., Bau, M., 2019. Regional variations in fluid formation and metal sources in MVT mineralization in the Pennine Orefield, UK: Implications from rare earth element and yttrium distribution, Sr-Nd isotopes and fluid inclusion compositions of hydrothermal vein fluorites. Ore Geol. Rev. 107: 960–72. https://doi.org/10.1016/j.oregeorev.2019.03.014

Lafuente, B., Downs, R.T., Yang, H., Stone, N., 2015. The power of databases: the RRUFF project. In: Highlights in Mineralogical Crystallography, T Armbruster and R M Danisi, eds. Berlin, Germany, W. De Gruyter, pp 1-30.

Land, L.S., 1980. The isotopic and trace element geochemistry of dolomite: the state of the art, in Zenger et al., eds., Concepts and models of dolomitization: Society of Economic Paleontologists and Mineralogists, Special Publication, 28, 87–110.

Laville, E., 1985. Evolution sédimentaire, tectonique et magmatique du bassin jurassique du Haut Atlas (Maroc): Modèle en relais multiples de décrochement (Thèse), Sci, Montpellier pp. 166 (in French).

Laville, E., 1988. Multiple releasing and restraining stepover model for the Jurassic strikeslip basin of the Central High Atlas (Morocco). In: Manspeizer, W. (Ed.), Triassic-Jurassic rifting. Continental Breakup and the Origins of the Atlantic Passive Margins. Dev. in Geotect 22, (21), pp. 1–25 (Amsterdam).

Laville, E., Harmand, C., 1982. Evolution magmatique et tectonique du bassin intracontinental mésozoïque du Haut Atlas (Maroc): un modèle de mise en place synsédimentaire de massifs “anorogéniques” liés à des décrochements, Bull. Soc. Géol. Fr. XXIV 2: 213–227 (in French).

Laville, E., Pique, A., Amrhar, M., Charroud, M., 2004. A restatement of the mesozoic Atlasic rifting (Morocco). J. Afr. Earth Sci. 38, 145–153. https://doi.org/10.1016/j. jafrearsci.2003.12.003.

Lhachmi, A., Lorand, J.P., Fabriès, J., 2001. Pétrologie de l’intrusion alcaline Mésozoïque de la région d’Anemzi, Haut Atlas central. Maroc. J. Afr. Earth Sci. 32, 741–764.

Lüders, V., Romer, R.L., Gilg, H.A., Bodnar, R.J., Pettke, T., Misantoni, D., 2009. A geochemical study of the Sweet Home Mine, Colorado Mineral Belt, USA: hydrothermal fluid evolution above a hypothesized granite cupola. Miner. Deposita 44, 415-434. https://doi.org/10.1007/s00126-008-0221-3.

Mangler, M.F., Marks, M.A.W., Zaitzev, A.N., Eby, G.N., Markl, G., 2014. Halogen (F, Cl, and Br) at Oldoinyo Lengai volcano (Tanzania): Effects of magmatic differentiation, silicate–natrocarbonatite Melt separation and surface alteration of natrocarbonatite. Chem. Geol. 365, 43–53.

Margoum, D., Bouabdellah, M., Klügel, A., Banks, D.A., Castorina, F., Cuney, M., Jébrak, M., Gulcan Bozkaya, G., 2015. Pangea rifting and onward pre-Central Atlantic opening as the main ore-forming processes for the genesis of the Aouli REE-rich fluorite-barite vein system, Upper Moulouya District. Morocco. J. Afr. Earth Sci. 108, 22–39.

Marks, M.A.W., Shilling, J., Coulson, I.M., Wenzel, T., Markl, G., 2008. The alkaline-peralkaline Tamazeght complex, High Atlas Mountains, Morocco: Mineral chemistry and petrological constraints for derivation from a compositionally heterogeneous mantle source. J. Petrol. 49, 1097-1131.

Marks, M.A.W., Neukirchen, F., Vennemann, T., Markl, G., 2009. Textural, chemical, and isotopic effects of late-magmatic carbonatitic fluids in the carbonatite–syenite Tamazeght complex, High Atlas Mountains, Morocco. Min. Pet. 97, 23–42.

Missenard, Y., Zeyen, H., Frizon de Lamotte, D., Leturmy P., Petit, C., Sébrier, M., Saddiqi, O., 2016. Crustal versus asthenospheric origin of the relief of the Atlas Mountains of Morocco. J. Geophys. Res. 111 (B03401) doi:10.1029/2005JB003708.

Moncada, D., Mutchler, S., Nieto, A., Reynolds, T.J., Rimstidt, J.D., Bodnar, R.J., 2012. Mineral Textures and Fluid Inclusion Petrography of the Epithermal Ag-Au Deposits at Guanajuato, Mexico. Application to Exploration. J. Geochem. Explor. 114, 20-35, Doi:10.1016/j.gexplo.2011.12.001.

Möller, P., Giese, U., Dulski, P., 1994. Behaviour of REE in alteration processes of granites. In: Seltman, R., Kämpf, H., Möller, P. (Eds.), Metallogeny of Collisional Orogens. Czech Geological Survey, Prague, pp. 368–374.

Mouguina, E.M., 2004. Les minéralisations polymétalliques (Zn-Pb, Cu, Co, Ni) du Jurassique du Haut Atlas central (Maroc): Contexte géodynamique, typologies et modèles génétiques (Dissertation), Faculté des Sciences Semlalia, Marrakech, 340 pp.

Munoz, M., Boyce, A.J., Courjault-Radé, P., Fallick, A.E., Tollon, F., 1999. Continental basinal origin of ore fluids from southwestern Massif Central fluorite veins (Albigeois, France): evidence from fluid inclusion and stable isotope analyses. Appl. Geochem. 14, 447–458.

Munoz, M., Premo, W.R., Courjault-Radé, P., 2005. Sm–Nd dating of fluorite from the worldclass Montroc fluorite deposit, southern Massif Central, France. Miner. Deposita 39, 970–975. https://doi.org/10.1007/s00126-004-0453-9.

N'da, A.B., Bouchaou, L., Reichert, B., Hanich, L., Ait Brahim, Y., Chehbouni, A.V., Beraaouz, E.H., Michelot, J.L., 2016. Isotopic signatures for the assessment of snow water resources in the Moroccan High Atlas Mountains: Contribution to Surface and Groundwater Recharge. Environ. Earth. Sci. 75,755. Doi 10.1007/s12665-016-5566-9.

Nadoll, P., Sośnicka, M., Kraemer, D., Duschl, F., 2019. Post-Variscan structurally-controlled hydrothermal Zn-Fe-Pb sulfide and F-Ba mineralization in deep-seated Paleozoic units of the North German Basin: A review. Ore Geol. Rev. 106, 273–299. https://doi.org/10.1016/j.oregeorev.2019.01.022.

Rowan, E.L., Thibiéroz, J., Bethke, C.M., de Marsily, G., 1996. Geochemical and hydrologic conditions for fluorite mineralization in regions of continental extension: An example from the Albigeois district, France, in Sangster, D. F., Ed., Carbonate-hosted lead-zinc deposits: Society of Economic Geologists, Special Publication Number 4, p. 448-464. https://doi.org/10.5382/SP.04.34.

Partey, F., Lev, S., Casey, R., Widom, E., Lueth, V.W., Rakovan, J., 2009. Source of fluorine and petrogenesis of the Rio Grande rift-type barite-fluorite-galena deposits. Econ. Geol. 104 (4), 505–520.

Pi, T., Solé, J., Golzarri, J.I, Richards, J., Espinosa, G., 2007. Autoradiography of geological fluorite samples for determination of uranium and thorium distribution using nuclear track methodology. Revista Mexicana De Física S53 (3) 57–60.

Piqué, A., Michard, A., 1989. Moroccan Hercynides: a synopsis. The Paleozoic sedimentary and tectonic evolution at the northern margin of West Africa. Am. J. Sci. 289, 286–330.

Rddad, L., Mouguina, E.M., Muchez, P., Darling, R.S., 2018. The genesis of the Ali Ou Daoud Jurassic carbonate Zn-Pb Mississippi Valley type deposit, Moroccan central High Atlas: constraints from bulk stable C-O-S, in situ radiogenic Pb isotopes, and fluid inclusion studies. Ore Geol. Rev. 99, 365–379. https://doi.org/10.1016/j. oregeorev.2018.06.020.

Rddad, L., 2021. The genesis of the Jurassic-hosted Mississippi Valley-Type Pb-Zn ore deposit, Tigrinine-Taabast district (Central High Atlas, Morocco): Insights from fluid inclusion and C-O-S-Pb isotopes studies. J. Afr. Earth Sci. 174. 104071.

Rddad, L., Mouguina, E.M., 2021. Sulfur and lead isotopic compositions of ore sulfides and mining economic potential of the High Atlas Mississippi Valley-type ore province, Morocco. J. Geochem. Explor. 226, 106765

Roedder, E., 1984. Fluid inclusions: Reviews in Mineralogy and Geochemistry, v. 12, 644 p.

Rollinson, H.R., 1993. Using geochemical data: Evaluation, presentation, interpretation. Longman Scientific and Technical, Wiley, New York, 352.

Saddiqi, O., El Haimer, F.Z., Michard, A., Barbarand, J., Ruiz, G.M.H., Mansour, E.M., et al., 2009. Apatite fission-track analyses on basement granites from south-western Meseta, Morocco: Paleogeographic implications and interpretation of AFT age discrepancies. Tectonophysics 475, 29–37.

Sadki, D., Sha, J.G., 2018. Jurassic reef events in the Moroccan Atlas: A review, Palaeoworld, 27, (4), 458-466. https://doi.org/10.1016/j.palwor.2018.08.001.

Salvi, S., Williams-Jones, A.E., 1990. The role of hydrothermal processes in the granite hosted Zr, Y, REE deposit at Strange Lake, Quebec/Labrador: Evidence from fluid inclusions: Geochim. Cosmochim. Acta 54, 2403–241

Salvi, S., Fontan, F., Monchoux, P., Williams-Jones, A.E., Moine, B., 2000. Hydrothermal mobilization of high field strength elements in alkaline igneous systems: evidence from the Tamazert Complex (Morocco). Econ. Geol. 95, 559-576.

Sami, M., El Monsef, M.A., Abart, R., Toksoy-Köksal, F., Abdelfadil, K.M., 2022. Unraveling the genesis of highly fractionated rare-metal granites in the Nubian Shield via the Rare-Earth Elements tetrad effect, Sr–Nd isotope systematics, and mineral chemistry. ACS Earth and Space Chemistry, 6(10), 2368-2384.

Sami, M., Theodoros, N., Farahat, E.S., Mohamed, H.A., Ahmed, A.F., Hauzenberger, C., 2017. Mineralogical, geochemical and Sr-Nd isotopes characteristics of fluorite-bearing granites in the Northern Arabian-Nubian Shield, Egypt: Constraints on petrogenesis and evolution of their associated rare metal mineralization. Ore Geol. Rev. 88: 1-22. https://doi.org/10.1016/j.oregeorev.2017.04.015.

Simonetti, A., Bell, K., 1995. Nd, Sr and Pb isotope systematics of fluorite at the Amba Dongar carbonatite complex, India: Evidence for hydrothermal and crustal fluid mixing. Econ. Geol. 90, 2018–2027.

Sizaret, S., Marcoux, E., Jébrak, M., Touray, J.C., 2004. The Rossignol fluorite vein, Chaillac, France, Multiphase Hydrothermal Activity and Intravein Sedimentation. Econ. Geol. 99, 1107-1122. https://doi.org/10.2113/gsecongeo.99.6.1107.

Sośnicka, M., Lüders, V., 2019. Super-deep, TSR-controlled Phanerozoic MVT type Zn-Pb deposits hosted by Zechstein-2 gas reservoir carbonate (Ca2), Lower Saxony Basin, Germany. Chem. Geol. Advances in Fluid and Melt Inclusion Research 508, 62–77. https://doi.org/10.1016/j.chemgeo.2018.04.025.

Sośnicka, M., Rddad, L., Kraemer, D. 2021. Preliminary fluid inclusion study of fluorite deposits adjacent to the Tamazert alkaline igneous complex, Morocco. European current research on fluid and melt inclusions Abstract Book, e-CROFI Conference, June 28th to July 2nd.

Souissi, F., Dandurand, J.L., Fortuné, J.P., 1997. Thermal and chemical evolution of fluids during fluorite deposition in the Zaghouan province, north-eastern Tunisia. Miner. Deposita 32 (3), 257-270.

Srivastava, R.K., Banerjee, S., Longstaffe, F.J., Bhagat, S., Sinha, D.K., 2022. Stable isotopic study of carbonatites from the Pakkanadu Alkaline Complex, southern India: Constraints on carbonatite melt evolution and sub-solidus, high temperature fluid-rock interaction, Lithos. 430–431. https://doi.org/10.1016/j.lithos.2022.106863.

Steele-MacInnis, M., Bodnar, R.J., Naden, J., 2011. Numerical model to determine the composition of H_2O–NaCl–$CaCl_2$ fluid inclusions based on microthermometric and microanalytical data. Geochim. Cosmochim. Acta 75, 21–40. https://doi.org/10.1016/j.gca.2010.10.002.

Sterner, S.M., Hall, D.L., Bodnar, R.J., 1988. Synthetic fluid inclusions. V. Solubility relations in the system NaCl-KCl-H_2O under vapor-saturated conditions: Geochim. Cosmochim. Acta 52, 989–1006.

Sverjensky, D.A., 1984. Europium redox equilibria in aqueous solution. Earth Planet. Sci. Lett. 67, 70–78.

Tapponier, P., 1977. Evolution tectonique du système Alpin en Méditerranée: Poinçonnement et écrasement rigide plastique. Bull. Soc. Geol. Fr. 177 (3), 437–460 (t. XIX) (in French).

Taylor, H.P., Jr., 1997. Oxygen and hydrogen isotope relationships in hydrothermal mineral deposits. In: Barnes HL (ed.) Geochemistry of hydrothermal ore Deposits, 3rd ed., pp. 229–302. New York, NY: Wiley.

Teixell, A.P., Ayarza., H., Zeyen., M., Fernandez, M., Arboleya, L., 2005. Effects of mantle upwelling in a compressional setting: The Atlas Mountains of Morocco. Terra Nova, 17, 456 – 461.

Tostevin, R., Shields, G.A., Tarbuck, G.M., He, T., Clarkson, M.O., Wood, R.A., 2016. Effective use of cerium anomalies as a redox proxy in carbonate-dominated marine settings. Chem. Geol. 438, 146–162. https://doi.org/10.1016/j.chemgeo.2016.06.027.

Tisserant, D., Thuizat, R., Agard, J., 1976. Données géochronologiques sur le complexe de roches alcalines du Tamazeght (Haut Atlas de Midelt, Maroc). Bull. Bur. Rech. Géol. Min. 3, 279–283.

Veizer, J., Hoefs, J., 1976. The nature of O^{18}/O^{16} and C^{13}/C^{12} secular trends in sedimentary carbonate rocks: Geochim. Cosmochim. Acta. 40 (11), 1387–1395.

Wang, L.X., Marks, M.A.W., Wenzel, T., Markl, G., 2014. Halogen-bearing minerals from the Tamazeght complex (Morocco): Constraints on halogen distribution and evolution in alkaline to Peralkaline magmatic systems. Canad. Mineral. 54,1347-1368. DOI:10.3749/canmin.1600007.

Wang, L., Tang, L., Zhang, S., Santosh, M., Pei, Q., Cao, H., Liu, F., 2020. Genesis of the Yujiadian F-Pb-Zn-Ag deposit, Inner Mongolia, NE China: Constraints from geochemistry, fluid inclusion, zircon geochronology and stable isotopes. Ore Geol. Rev. 122. 103528. https:// doi.org/10.1016/j.oregeorev.2020.103528.

Warme, J.E., 1988. Jurassic carbonate facies of the central and eastern High Atlas rift, Morocco. In: Jacobshagen, V. (Ed.), The Atlas System of Morocco. Lect. Notes Earth Sci, 15, pp. 169–199.

Webster, J.D., 1990. Partitioning of F between H_2O and CO_2 fluids and topaz rhyolite melt. Contr. Mineral. Petrol. 104, 424–438. https://doi.org/10.1007/BF01575620.

Williams-Jones, A.E., Samson, I.M., Olivo, G.R., 2000. The genesis of hydrothermal fluorite–REE deposits in the Gallinas Mountains, New Mexico. Econ. Geol. 95,327- 342.

Yaagoub, D., Hinaje, S., El Fartati, M., Gharmane, Y., Amrani, S., 2022. Cenozoic tectono-sedimentary evolution of the Upper Moulouya continental basins (Moroccan Atlas system): Insights from lithostratigraphy, structural analysis and paleostress reconstruction. J. Afric. Earth Sci. 196,104690. https://doi.org/10.1016/j.jafrearsci.2022.104690.

Zaitsev, A.N., Keller, J., Spratt, J., Perova, E.N., Kearsley, A., 2008. Nyerereite–pirssonite–calcite–shortite relationships in altered natrocarbonatites, Oldoinyo Lengai, Tanzania. Canad. Mineral. 46 (4), 843–860.

Zayane, R., Essaifi, A., Maury, R., Piqué, A., Laville, E., Bouabdelli, M., 2002. Cristallisation fractionnée et contamination crustale dans la série magmatique jurassique transitionnelle du Haut Atlas central (Maroc). C. R. Geoscience 334, 97–104 (in French).

Zappettini, E.O., Rubinstein, N., Crosta, S., Segal, S.J., 2017. Intracontinental rift-related deposits: A review of key models. Ore Geol. Rev. 89, 594-608.

FIGURES

Fig. 1. Map showing the Central and Oriental High Atlas with the location of the Tamazert fluorite ore deposits (redrawn and edited from the Moroccan Geological Map at a scale of 1/1,000,000 and modified after Rddad and Mouguina, 2021).

Fig. 2. Geologic map of the Eocene Tamazert igneous complex (modified after Agard, 1973; Kchit, 1990; Duggen et al., 2009; Bouabdellah et al., 2010) with the location of the investigated area (black rectangle).

Fig. 3. Geologic map displaying details of the investigated area shown in the inset of Figure 2 (black rectangle). It shows the location of the investigated fluorite-bearing ore deposits and the sites of collected samples in and around Tamazert complex, High Atlas, Morocco.

Fig. 4. Main lithostratigraphic column showing rock sequence, which hosts Tamazert fluorite ore deposits, High Atlas, Morocco. Numbers 1, 2 and 3 (pink circles) represent the fluorite ore deposits of Bou Imtessene, Tabeja, and Bou Izourane, respectively, High Atlas, Morocco

Fig. 5. Geologic cross sections showing the location of fluorite ore deposits: the Bou Imtessene (BTD), Bou Izourane (BZD), and Tabeja (TJD) in and around the Tamazert igneous complex, High Atlas, Morocco.

Fig. 6. Photomicrographs from syenite intrusion and associated skarn zone (a-f) and carbonate-hosted fluorite ore deposits (g-j). a) Syenite with alkali feldspar (Afs), aegirine (Aeg), pyroxene (Pyx), plagioclase (Pl), and subordinate chlorite, sample IM3, PPL; b) Syenite with aegirine (Aeg) and calcite (Ca-l) (sample TJ6), PPL; c) Skarn developed at the contact syenite-Jurassic limestone with abundant calcite (Ca-l) and subordinate wollastonite (Wo), sample TJ5, PPL; d) Skarn developed at the contact syenite-Jurassic limestone with calcite (Cal), clinopyroxene (Cpx), sample TJ4, XPL; e) Skarn with abundant plagioclase (Pl), alkali feldspar (Afs), calcite-1 (Ca-1), and interstitial fluorite-1 (F-1), PPL; f) Same photomicrograph as “e” in XPL; g) Purple fluorite (F-2) alternating with white fluorite (F-2) associated with iron oxides, Bou Izourane deposit, PPL; h) Veinlet of post ore calcite (Ca-3) crosscutting fluorite (F-2) vein, Bou Izourane deposit, XPL; i) Zoned purple fluorite (F-2), Tabeja deposit, PPL; j) Purple fluorite (F-2) associated with marls hosted in the Jurassic limestone, Tabeja deposit, PPL

Fig. 7. Photos of outcrops near the syenite-hosted Bou Imtessene ore deposit. a) Skarn developed at the contact between the syenite intrusion and the Jurassic limestone; b) Purple fluorite (F-1) disseminated within the skarn developed at the contact between the syenite and the Jurassic limestone; c) Vein of

purple fluorite (F-1a) associated with calcite (Ca-1a) and iron oxide hosted in syenite; d) Dike of lamprophyre crosscutting the contact zone and syenite.

Fig. 8. Photos of outcrops and hand specimens collected from the Bou Izourane fluorite deposit, which is hosted by Jurassic limestones. a) Fluorite (F-2) and calcite (Ca-2) replacing Jurassic limestone; b) Fluorite (F-2) and calcite (Ca-2) assemblage in the proximity of a NE-SW-trending fault, Bou Izourane ore deposit; c) Fluorite (F-2) in breccia associated with a reverse fault, the reactivation of which occurred after the deposition of the ore; d) Euhedral purple fluorite (F-2) associated with calcite (Ca-2); e) Zoned white and purple fluorite (F-2).

Fig. 9. Photos of outcrops and hand specimens collected from the Tabeja fluorite deposit, which is hosted by Jurassic carbonates. a) Karstic cavity filled with fluorite (F-2). Note the presence of blocks of limestone within the cavity; b) Fluorite (F-2) and calcite (Ca-2) in brecciated Jurassic limestone; c) Fluorite (F-2) and calcite (Ca-2) associated with iron oxides hosted in the Jurassic limestone; d) Fresh sample of purple fluorite (F-2) collected from the karstic cavity; e) Brecciated purple fluorite (F-2) and calcite (Ca-2) hosted in the Jurassic limestone and marl; and f) Purple fluorite (F-2) in vugs hosted in the altered Jurassic limestone.

Fig. 10. Microphotographs of fluid and solid inclusions in interstitial fluorites (F-1) hosted by altered syenite. a)Type 1 secondary trail of aqueous fluid inclusions (black arrows) crosscutting crystals of interstitial fluorite (sample IM13); b) Type 1 secondary 3-phase (L+V+S) aqueous inclusions with blurry content (inset) (sample IM13); c) alteration assemblage of fluorite and aegirine (Aeg), fluorite contains multiple elongated crystals causing radiation damage in the form of halos (sample IM13); d-e) Multi-ring and one-ring radiation damage halos in purple fluorite (samples IM15, IM14); and f) Yellowish relict mineral in the centre of the poorly-developed radiation damage halo.

Fig. 11. Raman spectrum of a shortite solid enclosed in a high salinity Type 1 fluid inclusion (P1_fi1) hosted in fluorite from the Bou Imtessene deposit (sample IM13). For a reference, the spectrum of shortite from the RRUFF database was used (in grey)

Fig. 12. Microphotographs of fluid inclusions hosted in fluorite (F-2) from carbonate-hosted Tabeja (a) and Bou Izourane (b-f) deposits. a) Spherical Type 2 primary two-phase (L+V) aqueous inclusions within the growth zone in banded purple-white fluorite (sample TJ1); b) Irregularly-shaped Type 2 primary two-phase (L+V) aqueous inclusions decorating a growth zone in banded purple-white fluorite (sample BZ1);

c) Growth zone containing prismatic Type 2 primary two-phase (L+V) aqueous inclusions as well as discrete trails of Type 3 pseudo-secondary two-phase (L+V) aqueous inclusions (marked by dotted lines), banded purple-white fluorite (sample BZ9); d) High -temperature Type 3 fluid inclusion trail, inset: rare three-phase ($L+L_{CO2}+V_{CO2}$) Type 3 inclusions, banded purple-white fluorite (sample BZ9); e) Darkened growth zones in white fluorite with boiling FIA's, inset: boiling FIA consisting of co-existing aqueous two-phase (L+V) and vapor (V) inclusions (sample BZ2); f) Growth zone containing flashing FIA consisting of vapor (V) inclusions, white fluorite (sample BZ2).

Fig. 13. Diagram presenting microthermometric data from three types of fluid inclusions (fi's) hosted in fluorite (F-1) and calcite (Ca-1) from altered syenite as well as carbonate-hosted deposits. For interpretation of the references to color in this figure's legend, the reader is referred to the web version of this article).

Fig. 14. The plot of $\delta^{13}C_{VPDB}$ vs $\delta^{18}O_{VSMOW}$ values for Jurassic limestones, carbonate-rich skarns, carbonatites, and calcites in the Tamazert ore deposits. The isotope values of marine carbonate (Hoefs, 2018; Veizer and Hoefs, 1976), primary carbonatite (Keller and Hoefs, 1995), igneous rocks (Hoefs, 2018; Hoefs, 2009; Ohmoto and Goldhaber, 1997), Tamazert carbonatites (Bouabdellah et al., 2010), and Cape Verde and Canary Islands carbonatites (Hoernle et al., 2002; Hoernle and Tilton, 1991) are added for comparison.

Fig. 15. Chondrite-normalized REY patterns of the country rocks (top), the fluorites (middle), and the calcites (bottom) from the Tamazert fluorite ore deposits. Chondrite values used for normalization are from Barrat et al. (2012).

Tables

Table 1. The analyzed minerals and country rocks in the Tamazert fluorite deposits.

Table 2. Carbon and oxygen isotopes of the host-rock limestone, skarn, carbonatite, and calcite in the Tamazert ore deposits

Table 3. REY and other trace elements data for fluorite, calcite, and the country rocks in the Tamazert ore deposits.

FIGURES

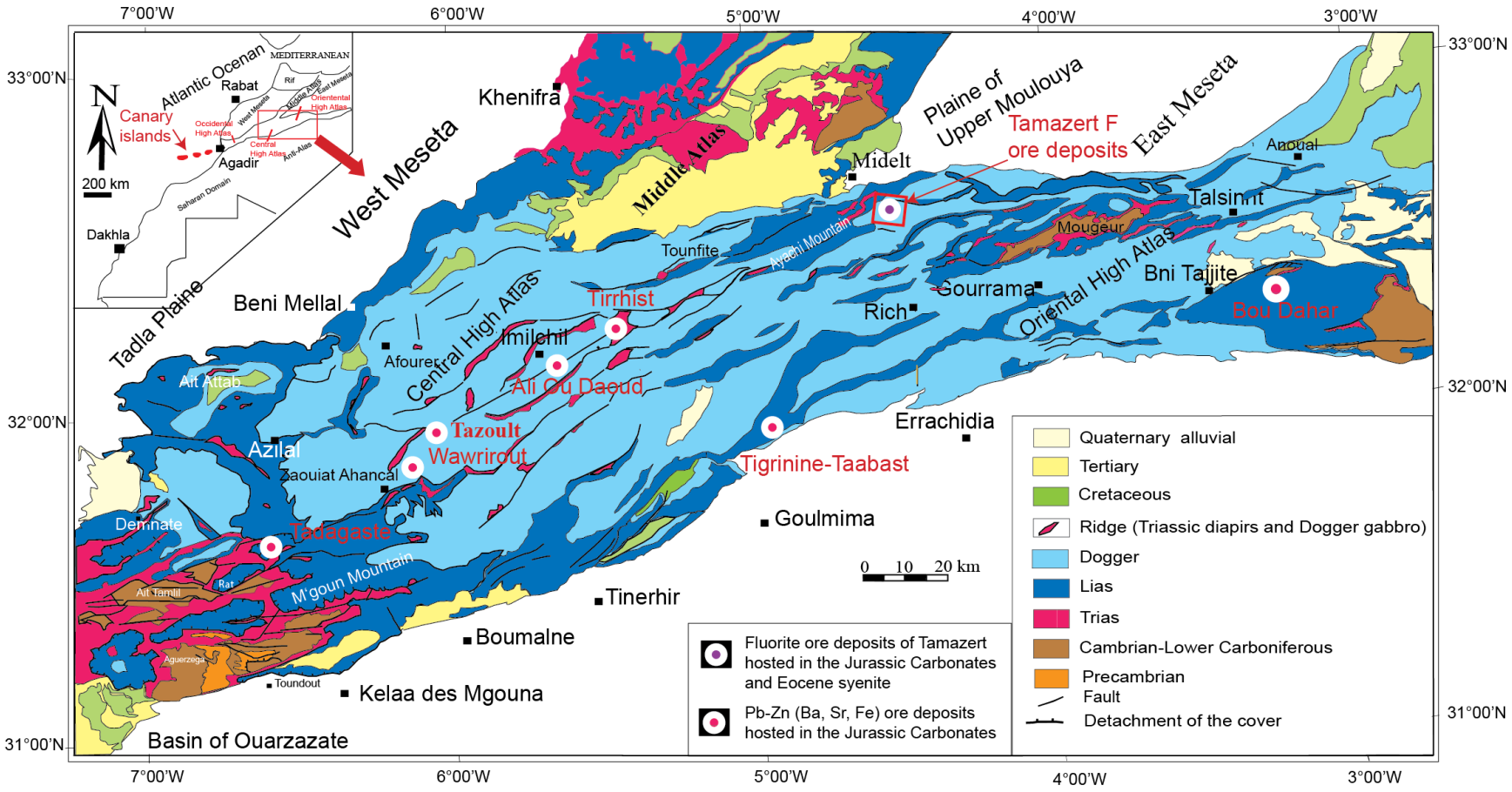

Fig 1

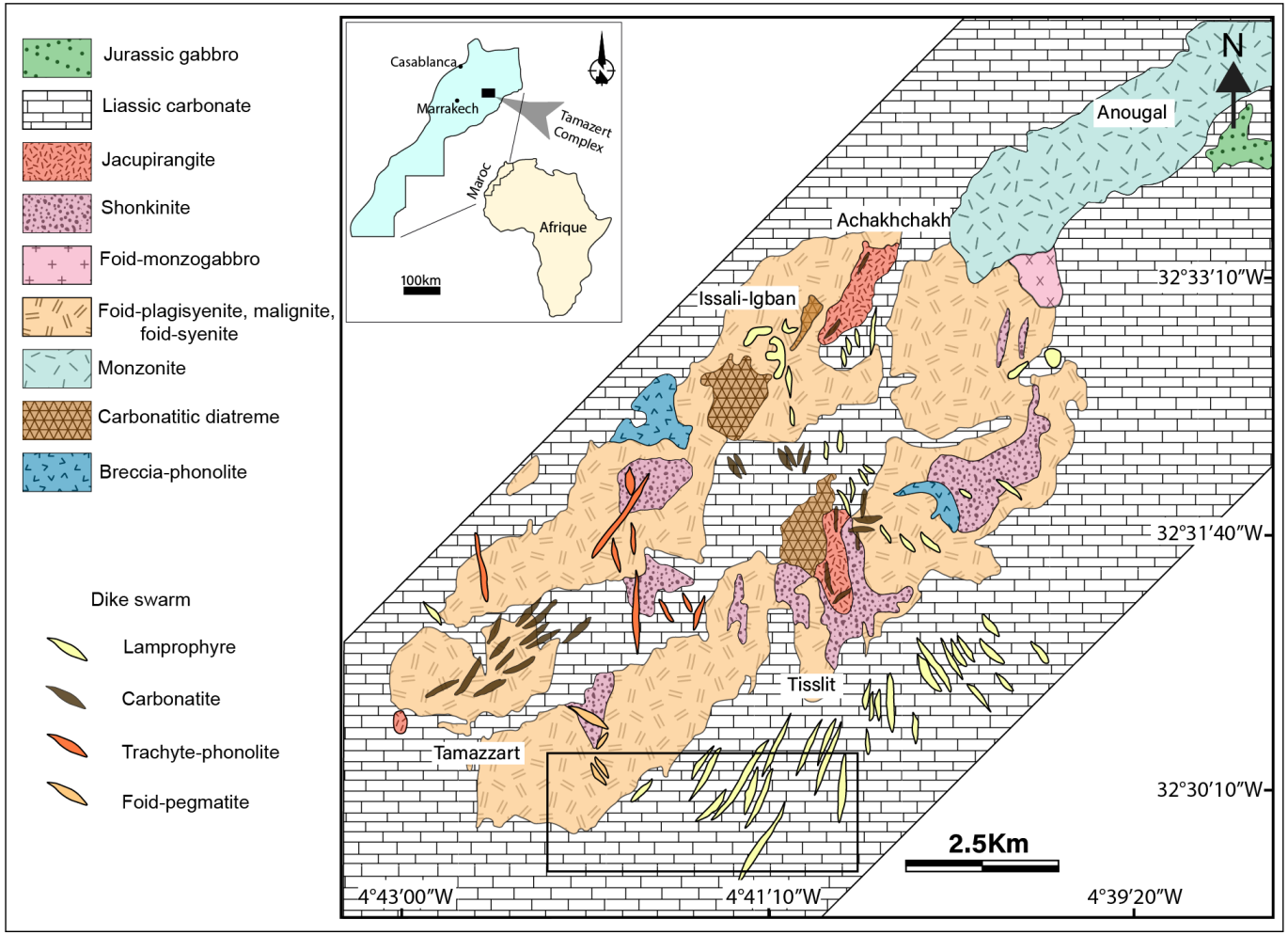
Jurassic gabbro
Liassic carbonate
Jacupirangite
Shonkinite
Foid-monzogabbro
Foid-plagisyenite, malignite, foid-syenite
Monzonite
Carbonatitic diatreme
Breccia-phonolite
Dike swarm
Lamprophyre
Carbonatite
Trachyte-phonolite
Foid-pegmatite
Casablanca
Marrakech
Tamazert Complex
Maroc
Afrique
100km
N
Anougal
Achakhchakh
Issali-Igban
Tisslit
Tamazzart
32°33′10″W
32°31′40″W
32°30′10″W
2.5Km
4°43′00″W
4°41′10″W
4°39′20″W

Fig. 2

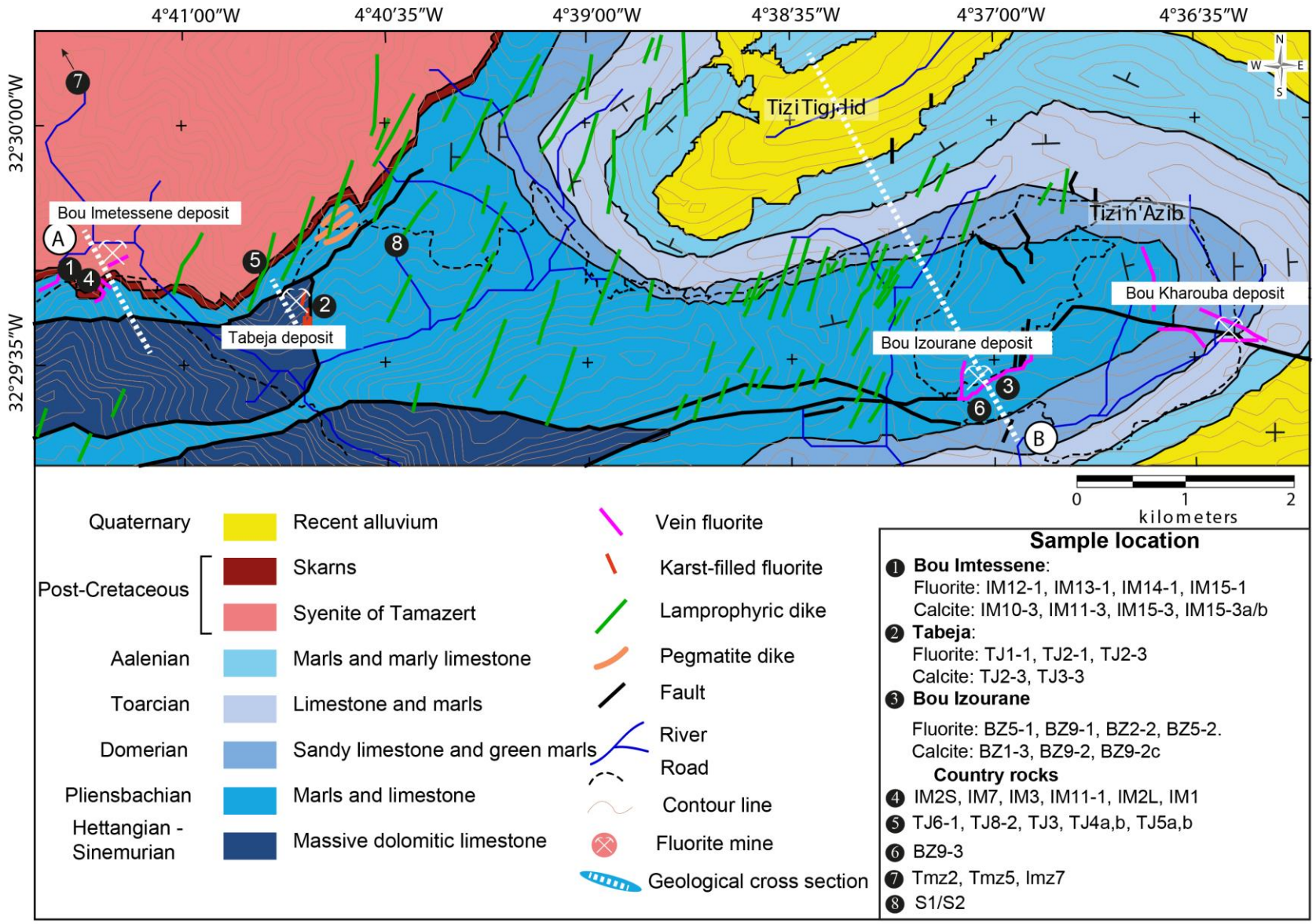
4°41′00″W
4°40′35″W
4°39′00″W
4°38′35″W
4°37′00″W
4°36′35″W
32°30′00″W
32°29′35″W
N
W
E
S
Bou Imetessene deposit
Tabeja deposit
Tizi Tigjdid
Tizi n'Azib
Bou Kharouba deposit
Bou Izourane deposit
A
B
0
1
2
kilometers
Quaternary
Recent alluvium
Post-Cretaceous
Skarns
Syenite of Tamazert
Aalenian
Marls and marly limestone
Toarcian
Limestone and marls
Domerian
Sandy limestone and green marls
Pliensbachian
Marls and limestone
Hettangian - Sinemurian
Massive dolomitic limestone
Vein fluorite
Karst-filled fluorite
Lamprophyric dike
Pegmatite dike
Fault
River
Road
Contour line
Fluorite mine
Geological cross section
Sample location
1 Bou Imtessene:
Fluorite: IM12-1, IM13-1, IM14-1, IM15-1
Calcite: IM10-3, IM11-3, IM15-3, IM15-3a/b
2 Tabeja:
Fluorite: TJ1-1, TJ2-1, TJ2-3
Calcite: TJ2-3, TJ3-3
3 Bou Izourane
Fluorite: BZ5-1, BZ9-1, BZ2-2, BZ5-2.
Calcite: BZ1-3, BZ9-2, BZ9-2c
Country rocks
4 IM2S, IM7, IM3, IM11-1, IM2L, IM1
5 TJ6-1, TJ8-2, TJ3, TJ4a,b, TJ5a,b
6 BZ9-3
7 Tmz2, Tmz5, Imz7
8 S1/S2

Fig 3

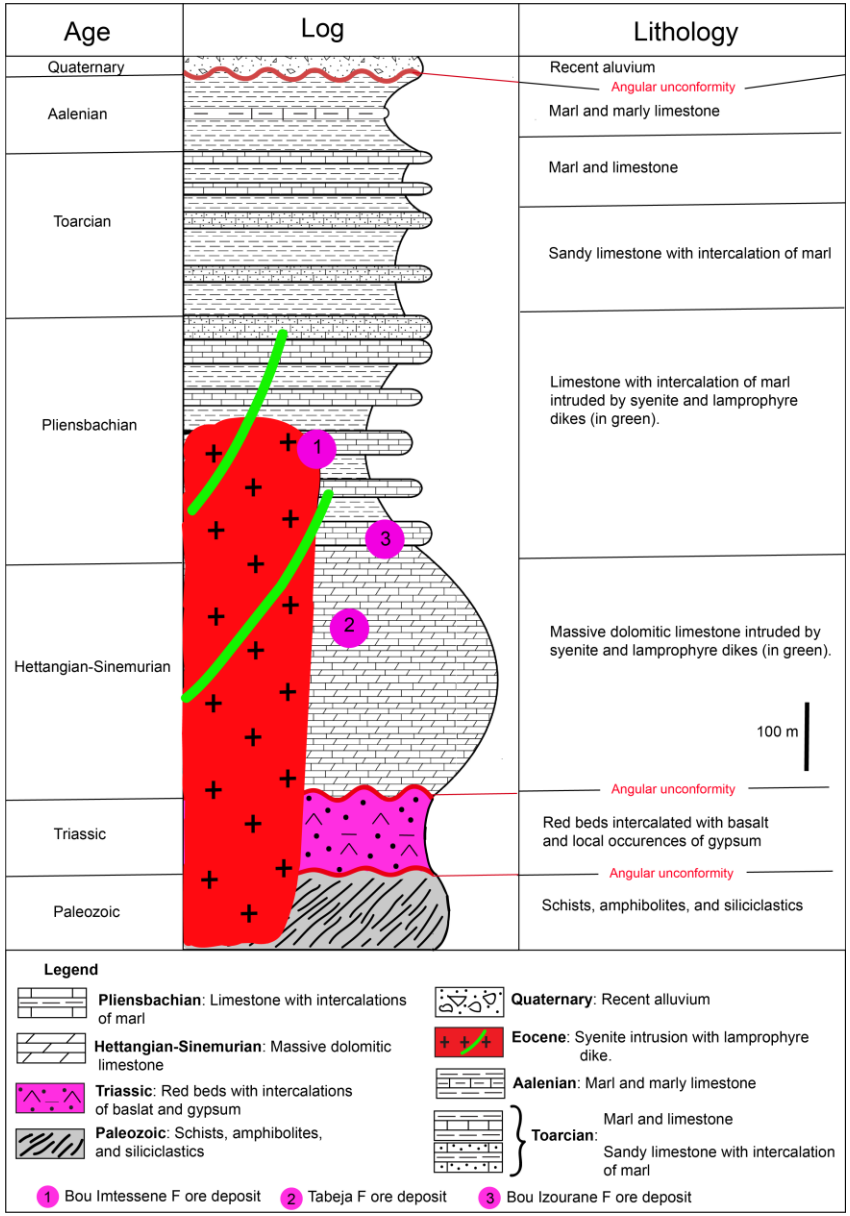
Age
Log
Lithology
Quaternary
Recent aluvium
Angular unconformity
Aalenian
Marl and marly limestone
Marl and limestone
Toarcian
Sandy limestone with intercalation of marl
Pliensbachian
Limestone with intercalation of marl intruded by syenite and lamprophyre dikes (in green).
1
2
3
Hettangian-Sinemurian
Massive dolomitic limestone intruded by syenite and lamprophyre dikes (in green).
100 m
Angular unconformity
Triassic
Red beds intercalated with basalt and local occurences of gypsum
Angular unconformity
Paleozoic
Schists, amphibolites, and siliciclastics
Legend
Pliensbachian: Limestone with intercalations of marl
Hettangian-Sinemurian: Massive dolomitic limestone
Triassic: Red beds with intercalations of baslat and gypsum
Paleozoic: Schists, amphibolites, and siliciclastics
Quaternary: Recent alluvium
Eocene: Syenite intrusion with lamprophyre dike.
Aalenian: Marl and marly limestone
Toarcian:
Marl and limestone
Sandy limestone with intercalation of marl
1 Bou Imtessene F ore deposit
2 Tabeja F ore deposit
3 Bou Izourane F ore deposit

Fig 4

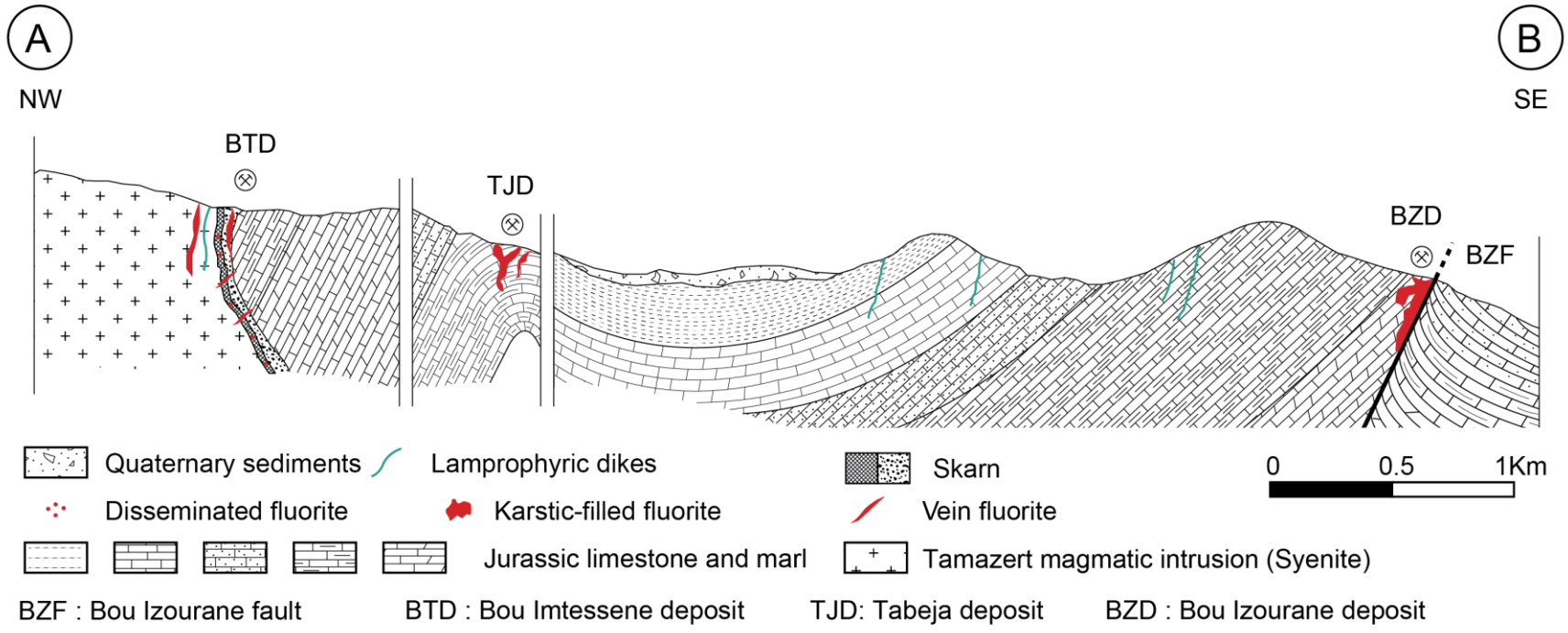
A
NW
B
SE
BTD
TJD
BZD
BZF
Quaternary sediments
Lamprophyric dikes
Skarn
0
0.5
1Km
Disseminated fluorite
Karstic-filled fluorite
Vein fluorite
Jurassic limestone and marl
Tamazert magmatic intrusion (Syenite)
BZF : Bou Izourane fault
BTD : Bou Imtessene deposit
TJD: Tabeja deposit
BZD : Bou Izourane deposit

Fig 5

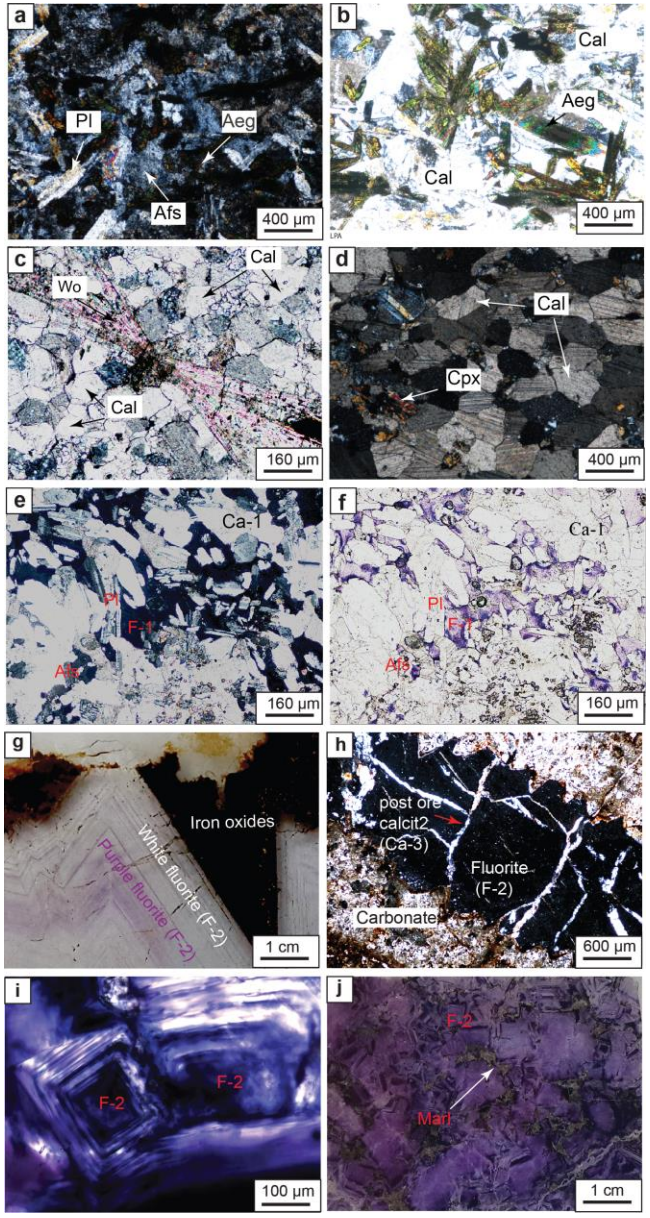
a
Pl
Aeg
Afs
400 µm
b
Cal
Aeg
Cal
400 µm
c
Wo
Cal
Cal
160 µm
d
Cal
Cpx
400 µm
e
Ca-1
Pl
F-1
Afs
160 µm
f
Ca-1
Pl
F-1
Afs
160 µm
g
Iron oxides
White fluorite (F-2)
Purple fluorite (F-2)
1 cm
h
post ore
calcit2
(Ca-3)
Fluorite
(F-2)
Carbonate
600 µm
i
F-2
F-2
100 µm
j
F-2
Marl
1 cm

Fig 6

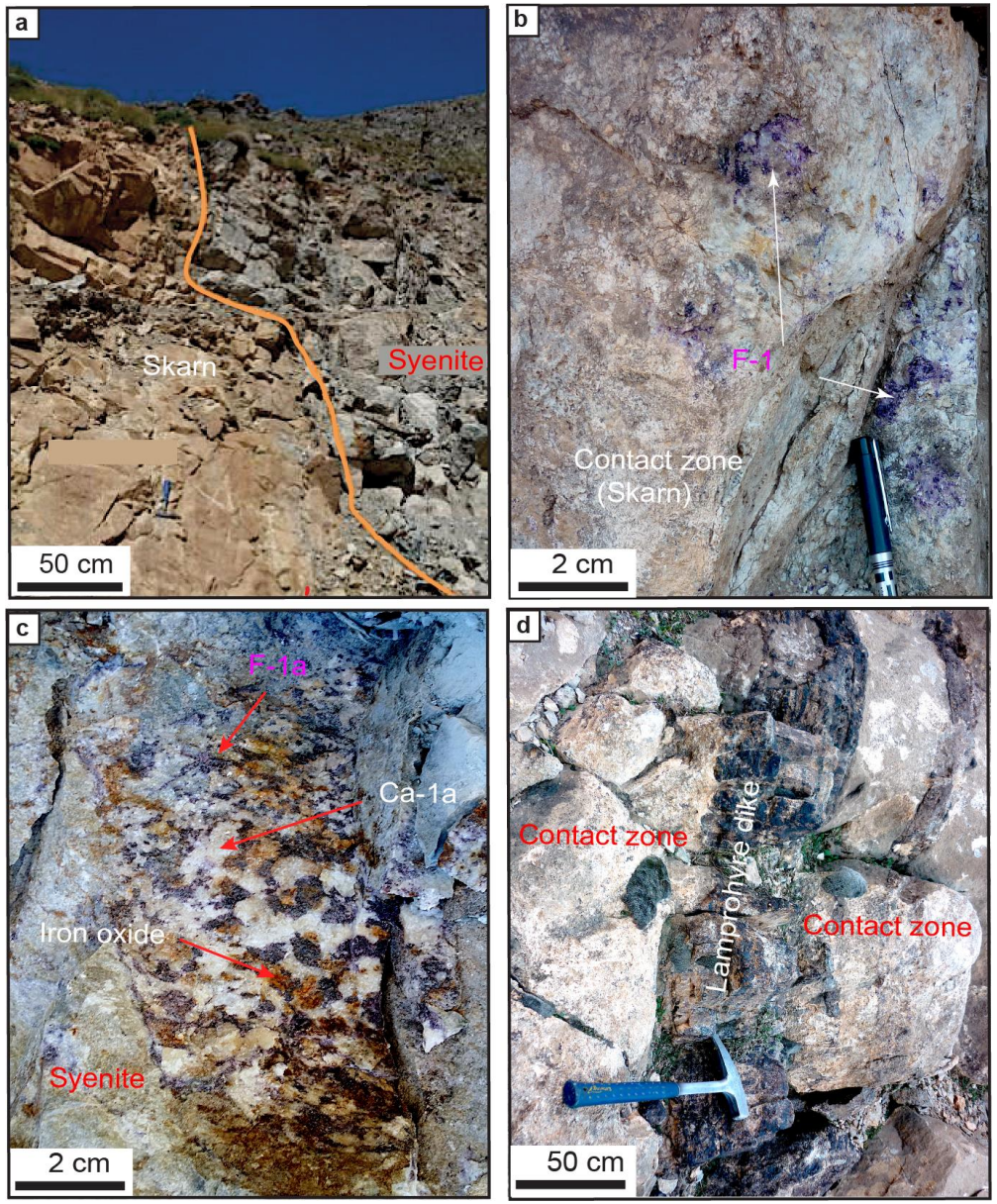
a
Skarn
Syenite
50 cm
b
F-1
Contact zone
(Skarn)
2 cm
c
F-1a
Ca-1a
Iron oxide
Syenite
2 cm
d
Contact zone
Lamprophyre dike
Contact zone
50 cm

Fig 7

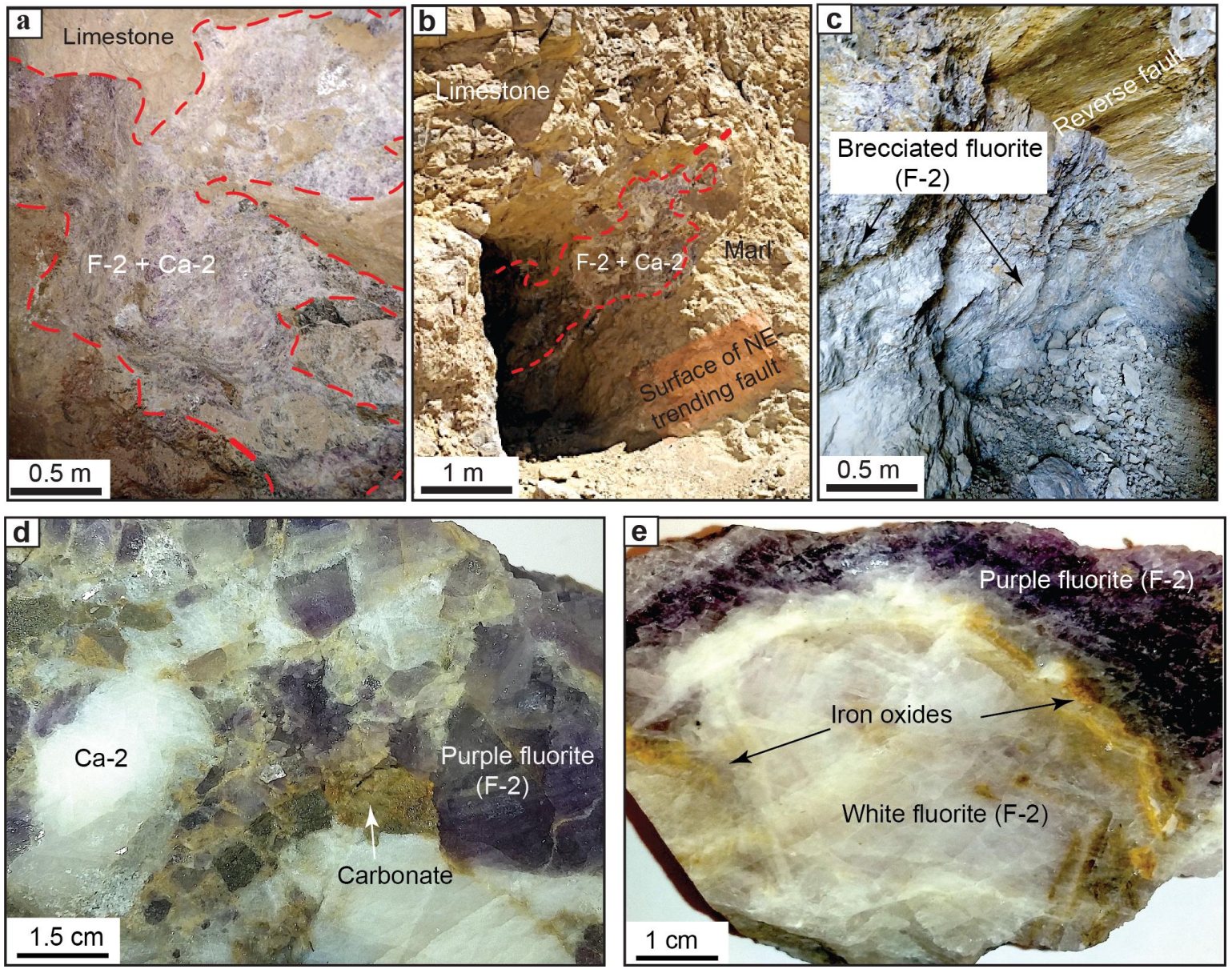
a
Limestone
F-2 + Ca-2
0.5 m
b
Limestone
F-2 + Ca-2
Marl
Surface of NE trending fault
1 m
c
Reverse fault
Brecciated fluorite (F-2)
0.5 m
d
Ca-2
Purple fluorite (F-2)
Carbonate
1.5 cm
e
Purple fluorite (F-2)
Iron oxides
White fluorite (F-2)
1 cm

Fig 8

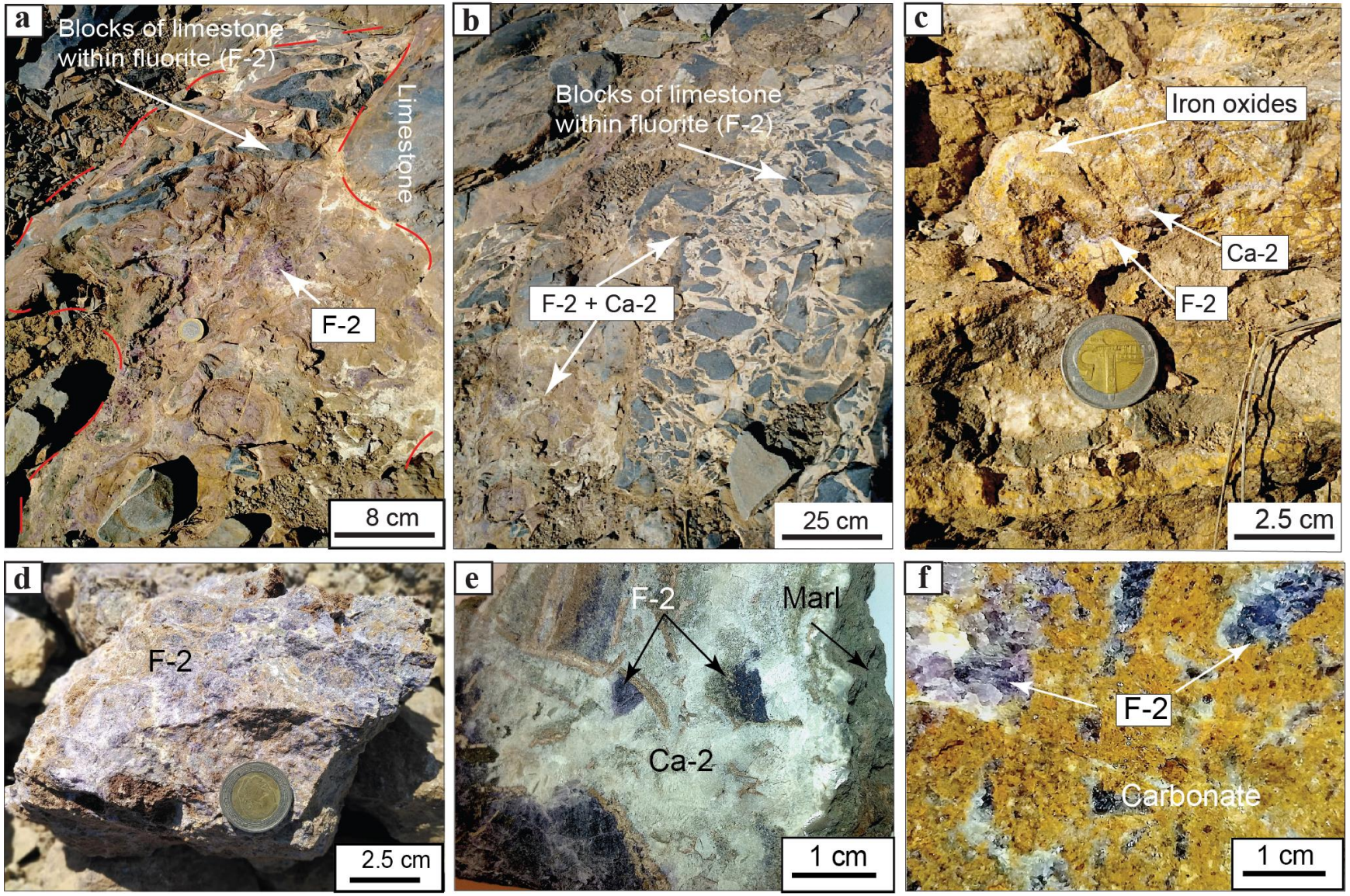
a
Blocks of limestone within fluorite (F-2)
Limestone
F-2
8 cm
b
Blocks of limestone within fluorite (F-2)
F-2 + Ca-2
25 cm
c
Iron oxides
Ca-2
F-2
2.5 cm
d
F-2
2.5 cm
e
F-2
Marl
Ca-2
1 cm
f
F-2
Carbonate
1 cm

Fig 9

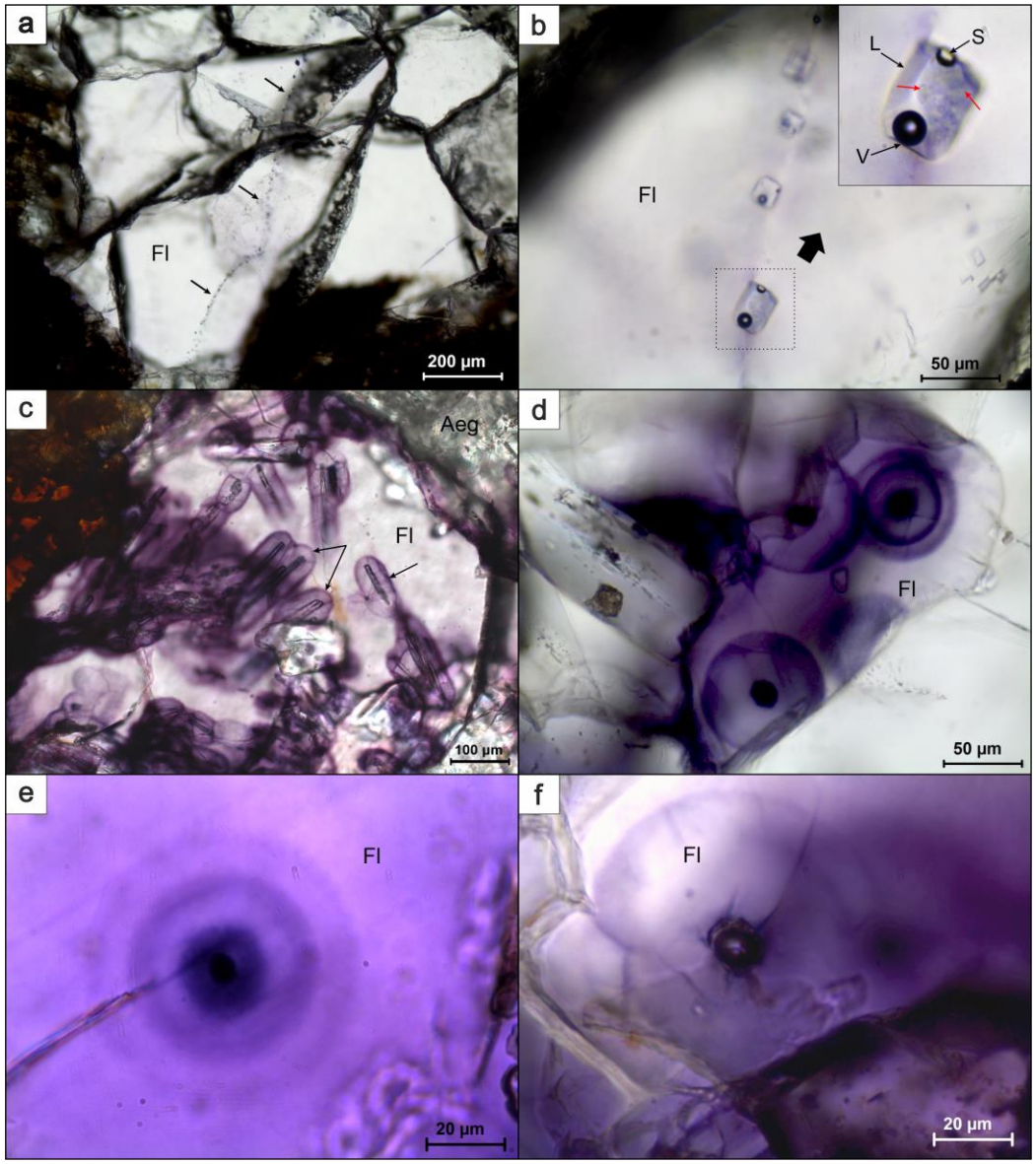
a
Fl
200 µm
b
L
S
V
Fl
50 µm
c
Aeg
Fl
100 µm
d
Fl
50 µm
e
Fl
20 µm
f
Fl
20 µm

Fig 10

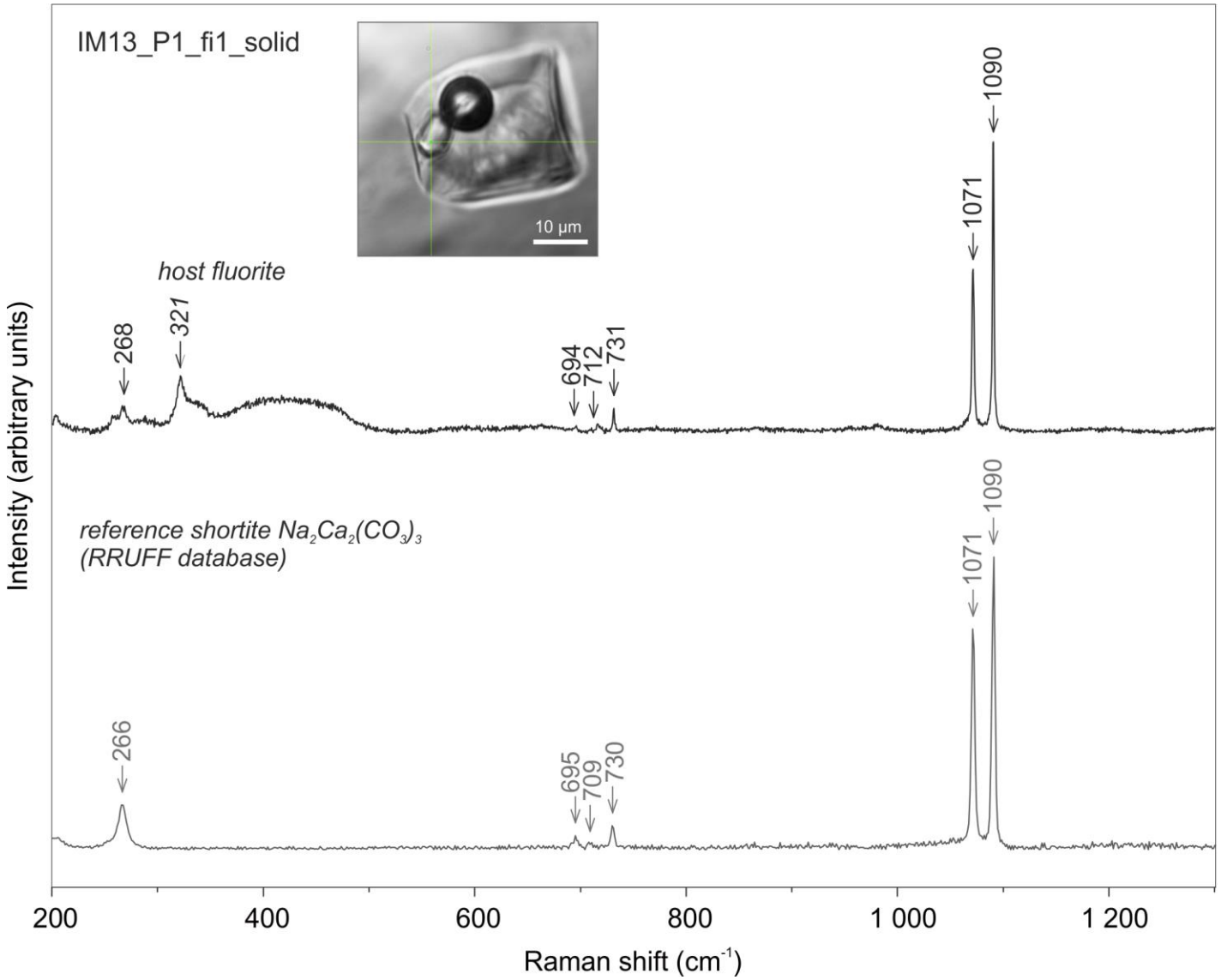
IM13_P1_fi1_solid
10 µm
host fluorite
268
321
694
712
731
1071
1090
reference shortite $Na_2Ca_2(CO_3)_3$
(RRUFF database)
266
695
709
730
1071
1090
Intensity (arbitrary units)
200
400
600
800
1 000
1 200
Raman shift (cm^{-1})

Fig 11

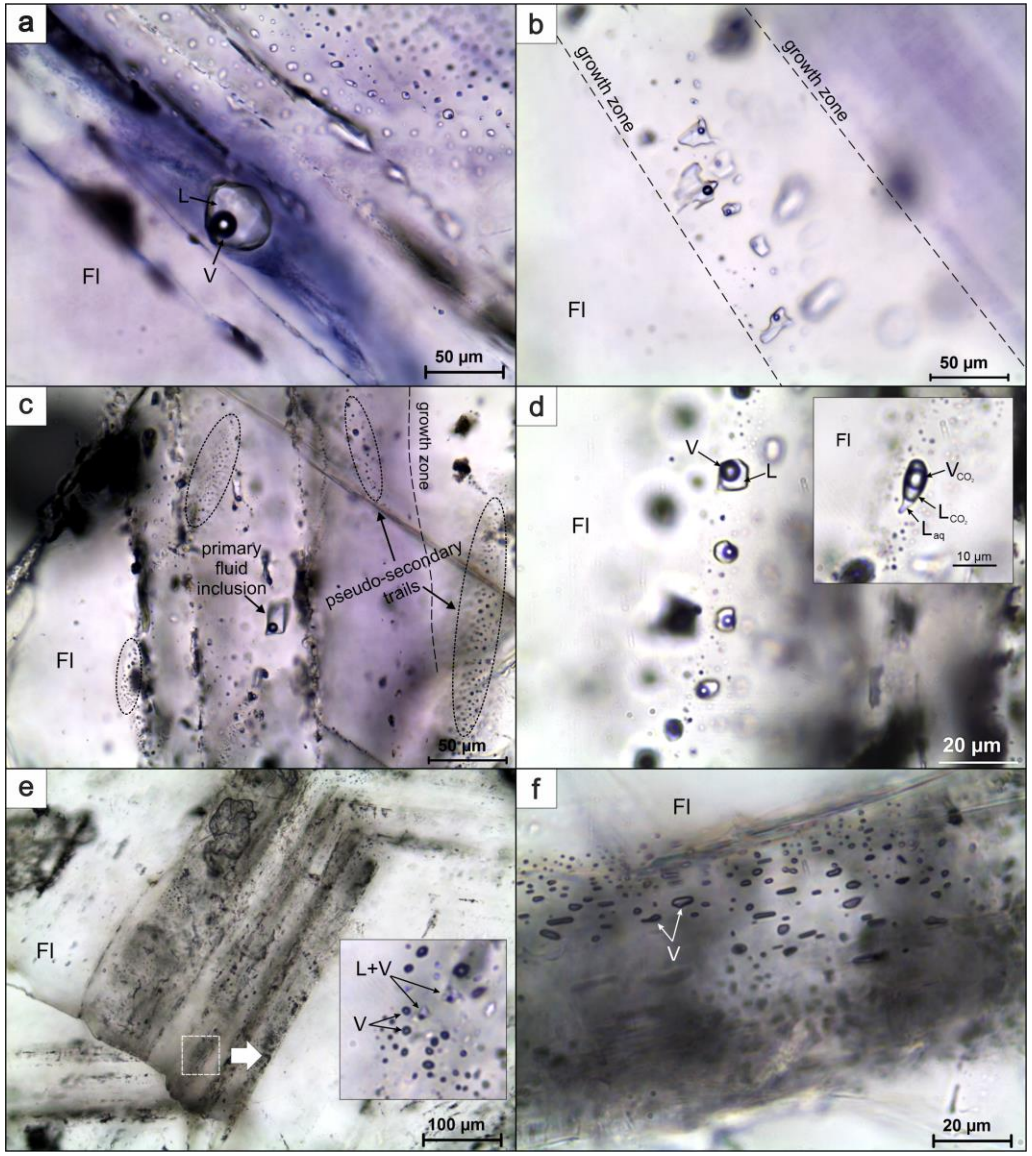
a
L
V
FI
50 µm
b
growth zone
growth zone
FI
50 µm
c
growth zone
primary fluid inclusion
pseudo-secondary trails
FI
50 µm
d
V
L
FI
V_{CO_2}
L_{CO_2}
L_{aq}
10 µm
20 µm
e
FI
L+V
V
100 µm
f
FI
V
20 µm

Fig 12

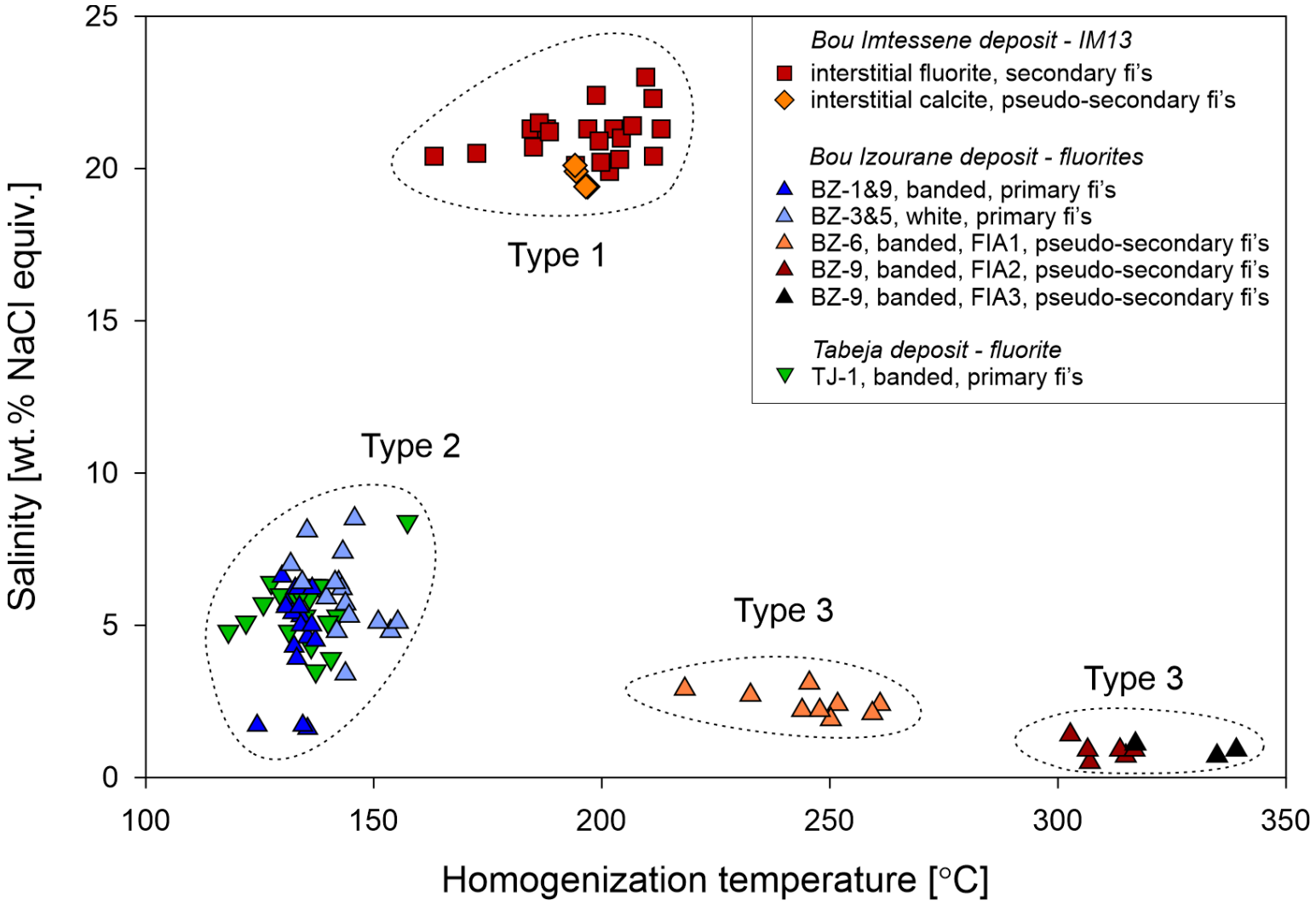
Bou Imtessene deposit - IM13
interstitial fluorite, secondary fi's
interstitial calcite, pseudo-secondary fi's
Bou Izourane deposit - fluorites
BZ-1&9, banded, primary fi's
BZ-3&5, white, primary fi's
BZ-6, banded, FIA1, pseudo-secondary fi's
BZ-9, banded, FIA2, pseudo-secondary fi's
BZ-9, banded, FIA3, pseudo-secondary fi's
Tabeja deposit - fluorite
TJ-1, banded, primary fi's
Type 1
Type 2
Type 3
Type 3
Salinity [wt.% NaCl equiv.]
Homogenization temperature [°C]
0
5
10
15
20
25
100
150
200
250
300
350

Fig. 13

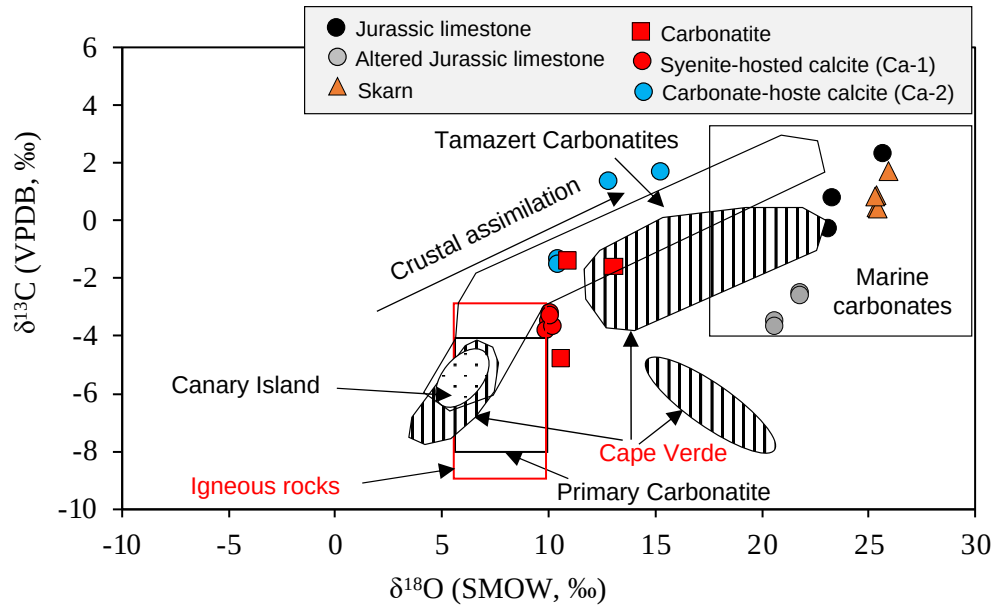
Jurassic limestone
Altered Jurassic limestone
Skarn
Carbonatite
Syenite-hosted calcite (Ca-1)
Carbonate-hoste calcite (Ca-2)
Tamazert Carbonatites
Crustal assimilation
Marine carbonates
Canary Island
Cape Verde
Igneous rocks
Primary Carbonatite
δ13C (VPDB, ‰)
δ18O (SMOW, ‰)
6
4
2
0
-2
-4
-6
-8
-10
-10
-5
0
5
10
15
20
25
30

Fig. 14

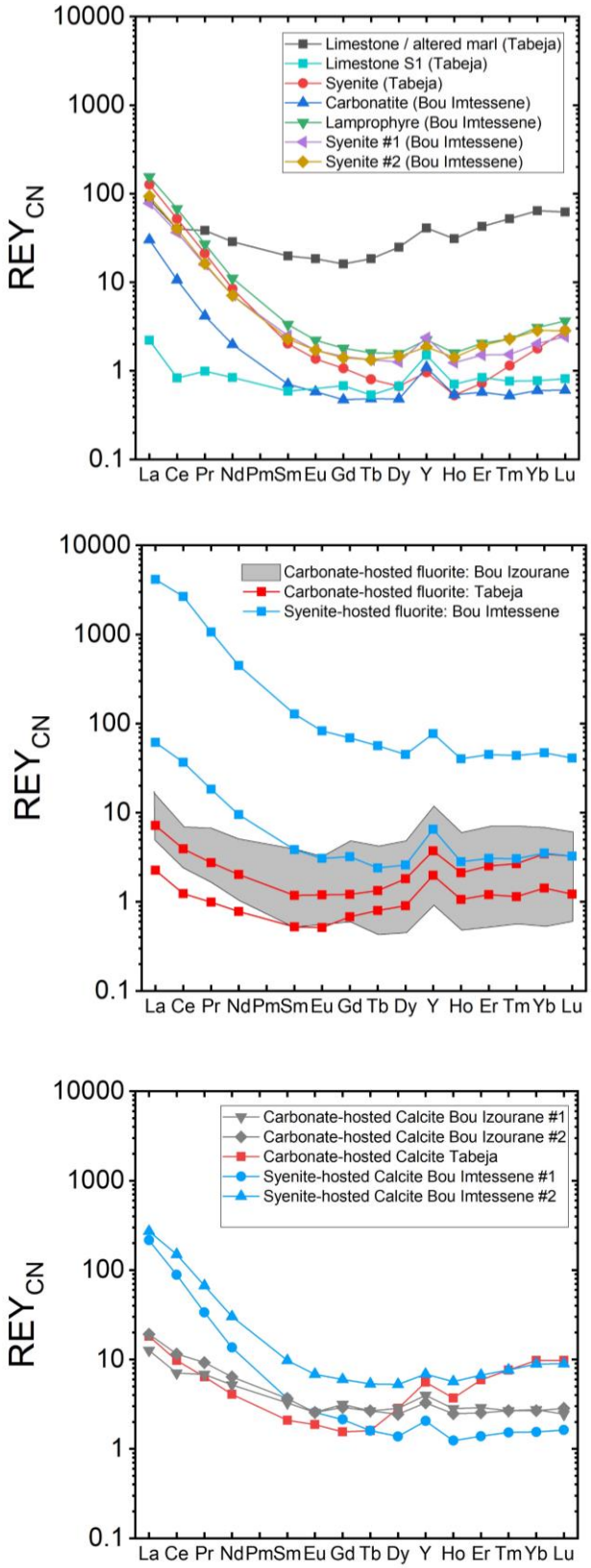
10000
1000
100
10
1
0.1
REY CN
Limestone / altered marl (Tabeja)
Limestone S1 (Tabeja)
Syenite (Tabeja)
Carbonatite (Bou Imtessene)
Lamprophyre (Bou Imtessene)
Syenite #1 (Bou Imtessene)
Syenite #2 (Bou Imtessene)
La Ce Pr Nd Pm Sm Eu Gd Tb Dy Y Ho Er Tm Yb Lu
Carbonate-hosted fluorite: Bou Izourane
Carbonate-hosted fluorite: Tabeja
Syenite-hosted fluorite: Bou Imtessene
Carbonate-hosted Calcite Bou Izourane #1
Carbonate-hosted Calcite Bou Izourane #2
Carbonate-hosted Calcite Tabeja
Syenite-hosted Calcite Bou Imtessene #1
Syenite-hosted Calcite Bou Imtessene #2

Fig. 15

Tables

Table 1

Samples	Locality	Description	Mode of occurrence and texture
Mineral			
IM12-1	Bou Imtessene	Purple fluorite (F-1)	Purple fluorite disseminated within the syenite
IM13-1	Bou Imtessene	Purple fluorite (F-1, Ca-1)	Purple fluorite and calcite disseminated within the syenite
IM15-1	Bou Imtessene	Purple fluorite (F-1)	Purple fluorite disseminated within the syenite
IM10-3	Bou Imtessene	Calcite (Ca-2)	Coarse-grained calcite in syenite rock with elongated Crystal
IM11-3	Bou Imtessene	Calcite (Ca-2)	Calcite viens in pegmatite with large biotite crystals
IM14-3	Bou Imtessene	Calcite (Ca-2)	Calcite associated with purple fluorite occurring as breccia hosted in syenite rock
IM15-3	Bou Imtessene	Calcite (Ca-2)	Coarse-graine calcite associated with purple fluorite hosted in syenite
TJ1-1	Tabeja	Purple fluorite (F-2)	Massive purple fluorite in karstic cavities in the Liassic limestone
TJ2-1	Tabeja	Purple fluorite (F-2)	Purple fluorite associated with calcite
TJ2-3	Tabeja	Calcite (Ca-2)	Calcite associated with purple fluorite
BZ5-1	Bou Izourane	Purple fluorite (F-2)	Corase-graine purple fluorite associated with calcite
BZ9-1	Bou Izourane	Purple fluorite (F-2)	Corase-graine purple fluorite and calcite hosted in the Liassic limestone
BZ2-2	Bou Izourane	White fluorite (F-2)	Banded fluorite with alternating purple and white fluorite
BZ5-2	Bou Izourane	White fluorite (F-2)	Coarse-graine white fluorite associated with calcite
BZ1-3	Bou Izourane	Calcite (Ca-2)	Corase-graine calcite associated with fluorite
BZ9-2	Bou Izourane	Calcite (Ca-2)	Calcite lining a fracture filled with purple fluorite
Whole rock			
IM2S	Bou Imtessene	Syenite	Coarse-grained texture syenite crosscut by Lamprophyre dyke
IM7	Bou Imtessene	Syenite	Coarse- grained syenite with phenocrusts and dessiminated fluorite
IM11-1	Bou Imtessene	Pegmatite	Pegmatite, associated with syenite, with large crystals of biotite and contains fluorite and calcite
IM2L	Bou Imtessene	Lamprophyre	Fine-graine texture lamprophyre dyke crosscutting syenite
IM1	Bou Imtessene	Skarn	Hosts disseminated fluorite
IMz2	Bou Imtessene	Carbonatite	Coarse-graine texture carbonatite outcropping North of the investigated area
IMz7	Bou Imtessene	Carbonatite	Coarse-graine texture carbonatite outcropping North of the investigated area
TJ6-1	West of Tabeja	Syenite	Coarse-grain texture syenite
TJ8-2	West of Tabeja	Pegmatite	Coarse-grain texture with large ellongated crystals
TJ4	West of Tabeja	Skarn	Calcite-rich contact zone with foliated-like structure
TJ2-4	Tabeja	Altered marl	Light green marls associated with fluorite and calcite
BZ9-3	Bou Izourane	Altered carbonate	Hydrothermally altered Liassic limestone
S1	Near Tabeja	Liassic limestone	Unaltered limestone far from igneous rocks and fluorite ore deposits
S2	Near Tabeja	Liassic Limestone	Unaltered limestone far from igneous rocks and fluorite ore deposits

Table 2

Samples	Location	Description	$\delta^{13}C$ (VPDB, ‰)	$\delta^{18}O$ (VPDB, ‰)	$\delta^{18}O$ (VSMOW, ‰)
S1	Near Tabeja	Limestone	0.8	-7.4	23.3
S2	Near Tabeja	Limestone	2.3	-5.0	25.7
TMz2	NW of Bou Imtessene	Carbonatite	-1.6	-17.3	13.1
TMz7	NW of Bou Imtessene	Carbonatite	-4.8	-19.7	10.6
TMz5	NW of Bou Imtessene	Carbonatite	-1.4	-19.4	10.9
BZ4	Bou Izourane	Altered limestone	-3.5	-10	20.6
BZ4b	Bou Izourane	Altered limestone	-3.7	-10	20.6
BZ9h	Bou Izourane	Altered limestone	-2.5	-9.1	21.8
BZ9hb	Bou Izourane	Altered limestone	-2.6	-8.8	21.8
IM1	Bou Imtessene	Skarn	1.7	-4.8	26.0
TJ4a	West of Tabeja	Skarn	0.5	-5.4	25.4
TJ4b	West of Tabeja	Skarn	0.4	-5.3	25.5
TJ5a	West of Tabeja	Skarn	0.9	-5.4	25.4
TJ5b	West of Tabeja	Skarn	0.8	-5.4	25.3
IM10-3	Bou Imtessene	Calcite-1	-3.5	-20.5	10
IM11-3	Bou Imtessene	Calcite-1	-3.8	-20.4	9.9
M14-3	Bou Imtessene	Calcite-1	-3.7	-20.1	10.2
IM15-3a	Bou Imtessene	Calcite-1	-3.2	-20.2	10.1
IM15-3b	Bou Imtessene	Calcite-1	-3.3	-20.5	10.1
TJ2-3	Tabeja	Calcite-2	-1.3	-19.9	10.4
TJ3-3	Tabeja	Calcite-2	-1.5	-19.9	10.4
BZ1-3	Bou Izourane	Calcite-2	1.7	-15.3	15.2
BZ9-2c	Bou Izourane	Calcite-2	1.4	-17.6	12.8

Table 3

	Bou Imtessene				Tabeja			Bou Izourane						
mg * kg^{-1}	Purple fluorite	Purple fluorite	Calcite	Calcite	Purple fluorite	Purple fluorite	Calcite	Purple fluorite	Purple fluorite	Purple fluorite	White fluorite	White fluorite	Calcite	Calcite
Element/Ref.	IM12-1	IM15-1	IM10-3	IM15-3	TJ1-1	TJ2-1	TJ2-3	BZ2-1	BZ5-1	BZ9-1	BZ2-2	BZ5-2	BZ1-3	BZ9-2
La	973.43	14.39	50.65	63.85	0.53	1.69	4.27	1.72	3.16	1.59	1.16	3.86	2.98	4.52
Ce	1592.97	22.04	53.09	89.75	0.74	2.35	5.87	2.17	4.16	2.17	1.41	3.53	4.23	6.91
Pr	96.81	1.67	3.06	6.08	0.09	0.25	0.58	0.29	0.60	0.40	0.15	0.33	0.62	0.84
Nd	207.55	4.41	6.31	13.98	0.36	0.94	1.90	1.19	2.33	1.91	0.47	0.98	2.41	2.97
Sm	19.52	0.59	0.56	1.49	0.08	0.18	0.32	0.24	0.48	0.59	0.08	0.14	0.50	0.56
Eu	4.84	0.18	0.15	0.40	0.03	0.07	0.11	0.07	0.14	0.19	BaO	0.05	0.15	0.15
Gd	14.22	0.66	0.44	1.23	0.14	0.25	0.32	0.33	0.67	0.98	0.12	0.17	0.65	0.60
Tb	2.12	0.09	0.06	0.20	0.03	0.05	0.06	0.05	0.12	0.16	0.02	0.03	0.10	0.10
Dy	11.41	0.66	0.35	1.34	0.23	0.46	0.72	0.37	0.81	1.22	0.11	0.18	0.72	0.62
Y	120.17	10.2	3.2	10.7	3.1	5.8	8.7	5.5	11.5	18.3	1.4	3.3	6.2	5.1
Ho	2.27	0.16	0.07	0.32	0.06	0.12	0.21	0.10	0.22	0.33	0.03	0.04	0.16	0.14
Er	7.45	0.51	0.23	1.11	0.20	0.42	0.98	0.33	0.73	1.16	0.09	0.15	0.48	0.42
Tm	1.15	0.08	0.04	0.20	0.03	0.07	0.20	0.04	0.10	0.18	0.01	0.02	0.07	0.07
Yb	7.88	0.59	0.26	1.50	0.24	0.58	1.64	0.32	0.69	1.15	0.09	0.12	0.46	0.45
Lu	1.01	0.08	0.04	0.22	0.03	0.08	0.24	0.05	0.10	0.15	0.01	0.02	0.06	0.07
∑REY	**3048.57**	**56.31**	**118.04**	**191.19**	**5.86**	**13.33**	**26.09**	**12.81**	**25.78**	**30.45**	**5.18**	**12.70**	**13.57**	**23.49**
Y/Ho	1.92	2.35	1.58	1.22	1.84	1.74	1.46	2.11	1.91	2.02	1.91	2.65	1.37	1.33
Ce/Ce*	1.05	1.04	1.06	1.01	0.88	1.02	0.98	0.91	0.79	0.76	0.87	0.96	0.78	0.87
Eu/Eu*	0.85	0.94	0.93	0.85	0.89	0.93	0.95	0.83	0.76	0.80	-	0.97	0.81	0.78
Y/Y*	0.17	3.07	4.51	0.73	6.16	2.75	0.99	4.27	1.74	1.15	14.59	12.08	1.89	2.10

Table 3 (Continued)

mg * kg^{-1}	Nepheline syenite	Syenite	Syenite	Pegmatite	Pegmatite	Lamprophyre	Carbonatite	Carbonatite	Limestone	Limestone	Altered carbonate	Marl	Skarn	Skarn
Element	IM2S	IM7	TJ6-1	IM11-1	TJ8-2	IM2L	TMZ2	TMZ7	S1	S2	BZ9-3	TJ2-4	IM1	TJ4
La	18.30	22.06	29.82	112.62	30.34	36.61	162.77	144.03	0.52	0.26	75.64	20.10	7.10	74.12
Ce	21.94	24.01	31.18	143.40	42.19	40.60	268.34	215.04	0.50	0.43	146.81	24.04	6.38	78.44
Pr	1.44	1.48	1.93	9.46	3.02	2.46	26.75	20.30	0.09	0.05	16.17	3.49	0.38	5.39
Nd	3.30	3.30	3.91	22.24	7.32	5.14	91.73	68.04	0.39	0.22	59.81	13.33	0.92	13.75
Sm	0.38	0.35	0.31	2.50	0.89	0.51	12.33	10.04	0.09	0.04	10.09	3.04	0.11	1.81
Eu	0.10	0.10	0.08	0.73	0.28	0.13	3.43	2.99	BaO	0.01	2.97	1.08	0.03	0.47
Gd	0.30	0.29	0.22	2.16	0.79	0.37	8.56	9.12	0.14	0.05	7.69	3.32	0.1	1.69
Tb	0.05	0.05	0.03	0.36	0.13	0.06	1.30	1.35	0.02	0.01	0.92	0.69	0.02	0.23
Dy	0.32	0.37	0.17	2.31	0.75	0.40	8.76	9.21	0.17	0.05	4.47	6.30	0.12	1.36
Y	3.7	2.9	1.5	17.8	5.6	3.5	52.41	41.90	2.34	0.48	18.3	64.0	1.7	10.6
Ho	0.07	0.08	0.03	0.53	0.15	0.09	1.65	1.59	0.04	0.01	0.74	1.76	0.03	0.26
Er	0.25	0.32	0.12	1.79	0.52	0.34	4.78	4.10	0.14	<d.l.	1.78	7.09	0.09	0.79
Tm	0.04	0.06	0.03	0.30	0.09	0.06	0.59	0.49	0.02	<d.l.	0.21	1.37	0.01	0.11
Yb	0.34	0.48	0.30	2.20	0.79	0.52	3.51	3.14	0.13	0.03	1.27	10.80	0.10	0.65
Lu	0.06	0.07	0.07	0.30	0.14	0.09	0.44	0.42	0.02	<d.l.	0.16	1.53	0.01	0.08
∑REY	50.26	55.67	69.49	316.54	92.23	90.48	647.35	531.76	4.61	1.64	347.01	161.98	17.03	189.75
Y/Ho	1.79	1.30	1.63	1.23	1.33	1.39	1.15	0.96	2.12	1.74	0.90	1.32	2.04	1.47
Ce/Ce*	1.04	1.08	0.97	1.06	1.01	1.02	1.02	1.06	0.72	1.13	1.00	0.78	1.22	1.10
Eu/Eu*	0.84	0.86	0.96	0.92	0.99	0.82	0.96	0.95	0.30	0.65	1.07	0.95	0.93	0.84
Y/Y*	4.71	2.68	8.70	0.46	1.68	2.75	0.16	0.15	10.07	-	0.33	0.12	14.27	1.24

.

Supplemetary Data - Fluid Inclusion Microthermometry

No	Deposit	Sample	Mineral	FIA	Inclusion no.	Shape	Size (µm)	Description	FIA description	Origin	Type	T_h	T_h mode	T_m (ice)	T_{fm}	Salinity (wt.% NaCl equiv.)
1	Bou Imtessene	IM13	interstitial fluorite	FIA1	fi1	prismatic	30	aqueous, 3phase	trail	secondary	Type 1	163	LVS→LS	-17.2	-46	20.4
2	Bou Imtessene	IM13	interstitial fluorite	FIA1	fi2	cubic	20	aqueous, 3phase	trail	secondary	Type 1	185	LV→L	-18.5	-48	21.3
3	Bou Imtessene	IM13	interstitial fluorite	FIA1	fi3	prismatic	15	aqueous, 3phase	trail	secondary	Type 1	197	LV→L	-18.4		21.3
4	Bou Imtessene	IM13	interstitial fluorite	FIA1	fi4	cubic	10	aqueous, 3phase	trail	secondary	Type 1	203	LV→L	-18.4		21.3
5	Bou Imtessene	IM13	interstitial fluorite	FIA1	fi5	prismatic	20	aqueous, 3phase	trail	secondary	Type 1	185	LV→L	-17.6	-49	20.7
6	Bou Imtessene	IM13	interstitial fluorite	FIA1	fi6	cubic	20	aqueous, 3phase	trail	secondary	Type 1	188	LV→L	-18.5	-49	21.3
7	Bou Imtessene	IM13	interstitial fluorite	FIA1	fi7	cubic	18	aqueous, 3phase	trail	secondary	Type 1	186	LV→L	-18.8		21.5
8	Bou Imtessene	IM13	interstitial fluorite	FIA2	fi1	negative crystal	25	aqueous, 3phase	trail	secondary	Type 1	173	LV→L	-17.4	-49	20.5
9	Bou Imtessene	IM13	interstitial fluorite	FIA2	fi2	cubic	10	aqueous, 3phase	trail	secondary	Type 1	211	LV→L	-17.3		20.4
10	Bou Imtessene	IM13	interstitial fluorite	FIA2	fi3	cubic	10	aqueous, 3phase	trail	secondary	Type 1	204	LV→L	-18		21.0
11	Bou Imtessene	IM13	interstitial fluorite	FIA2	fi4	negative crystal	12	aqueous, 3phase	trail	secondary	Type 1	202	LV→L	-16.6	-50	19.9
12	Bou Imtessene	IM13	interstitial fluorite	FIA2	fi5	negative crystal	15	aqueous, 3phase	trail	secondary	Type 1	207	LV→L	-18.6	-49	21.4
13	Bou Imtessene	IM13	interstitial fluorite	FIA2	fi6	negative crystal	10	aqueous, 3phase	trail	secondary	Type 1	213	LV→L	-18.5	-49	21.3
14	Bou Imtessene	IM13	interstitial fluorite	FIA3	fi1	negative crystal	10	aqueous, 3phase	trail	secondary	Type 1	200	LV→L	-17		20.2
15	Bou Imtessene	IM13	interstitial fluorite	FIA3	fi2	negative crystal	10	aqueous, 3phase	trail	secondary	Type 1	194	LV→L	-16.9		20.1
16	Bou Imtessene	IM13	interstitial fluorite	FIA3	fi3	negative crystal	10	aqueous, 3phase	trail	secondary	Type 1	204	LV→L	-17.1		20.3
17	Bou Imtessene	IM13	interstitial fluorite	FIA3	fi4	negative crystal	10	aqueous, 3phase	trail	secondary	Type 1	199	LV→L	-17.9		20.9
18	Bou Imtessene	IM13	purple interstitial fluorite	FIA4	fi1	cylindrical	10	aqueous, 3phase	trail	secondary	Type 1	189	LV→L	-18.3	-46	21.2
19	Bou Imtessene	IM13	purple interstitial fluorite	FIA4	fi2	prismatic	7	aqueous, 3phase	trail	secondary	Type 1	199	LV→L	-20		22.4
20	Bou Imtessene	IM13	purple interstitial fluorite	FIA4	fi3	spherical	6	aqueous, 3phase	trail	secondary	Type 1	211	LV→L	-19.9		22.3
21	Bou Imtessene	IM13	purple interstitial fluorite	FIA4	fi4	cylindrical	5	aqueous, 3phase	trail	secondary	Type 1	210	LV→L	-21		23.0
22	Bou Imtessene	IM13	interstitial calcite	FIA1	fi1	negative crystal	10	aqueous, 3phase	trail	secondary	Type 1	194	LV→L	-16.6	-49	19.9
23	Bou Imtessene	IM13	interstitial calcite	FIA1	fi2	negative crystal	10	aqueous, 3phase	trail	secondary	Type 1	197	LV→L	-15.9	-50	19.4

24	Bou Imtessene	IM13	interstitial calcite	FIA1	fi3	cubic	8	aqueous, 3phase	trail	secondary	Type 1	197	LV→L	-16		19.4
25	Bou Imtessene	IM13	interstitial calcite	FIA1	fi4	negative crystal	10	aqueous, 3phase	trail	secondary	Type 1	197	LV→L	-16		19.4
26	Bou Imtessene	IM13	interstitial calcite	FIA1	fi5	cubic	8	aqueous, 3phase	trail	secondary	Type 1	194	LV→L	-16.8		20.1
27	Tabeja	TJ1	purple fluorite	FIA1	fi1	spherical	50	aqueous, 2phase	growth zone	primary	Type 2	157.4	LV→L	-5.4		8.4
28	Tabeja	TJ1	purple fluorite	FIA1	fi2	spherical	10	aqueous, 2phase	growth zone	primary	Type 2	135	LV→L	-3.2		5.3
29	Tabeja	TJ1	purple fluorite	FIA1	fi3	spherical	11	aqueous, 2phase	growth zone	primary	Type 2	136.3	LV→L	-2.6		4.3
30	Tabeja	TJ1	purple fluorite	FIA1	fi4	spherical	9	aqueous, 2phase	growth zone	primary	Type 2	142	LV→L	-3.2		5.3
31	Tabeja	TJ1	purple fluorite	FIA1	fi5	spherical	10	aqueous, 2phase	growth zone	primary	Type 2	131.4	LV→L	-2.9		4.8
32	Tabeja	TJ1	purple fluorite	FIA1	fi6	spherical	10	aqueous, 2phase	growth zone	primary	Type 2	132.7	LV→L	-3.6		5.9
33	Tabeja	TJ1	purple fluorite	FIA2	fi1	negative crystal	23	aqueous, 2phase	growth zone	primary	Type 2	136.1	LV→L	-3.9		6.3
34	Tabeja	TJ1	purple fluorite	FIA2	fi2	negative crystal	30	aqueous, 2phase	growth zone	primary	Type 2	137.4	LV→L	-3.9		6.3
35	Tabeja	TJ1	purple fluorite	FIA2	fi3	spherical	19	aqueous, 2phase	growth zone	primary	Type 2	127.5	LV→L	-4		6.4
36	Tabeja	TJ1	purple fluorite	FIA2	fi4	cylindrical	25	aqueous, 3 phase	growth zone	primary	Type 2	137	LVS→LS	-3.9		6.3
37	Tabeja	TJ1	purple fluorite	FIA2	fi5	negative crystal	25	aqueous, 3 phase	growth zone	primary	Type 2	136.7	LVS→LS	-3.8		6.2
38	Tabeja	TJ1	purple fluorite	FIA2	fi6	cylindrical	30	aqueous, 3 phase	growth zone	primary	Type 2	135.9	LVS→LS	-3.6		5.9
39	Tabeja	TJ1	purple fluorite	FIA2	fi7	spherical	10	aqueous, 3 phase	growth zone	primary	Type 2	140.6	LVS→LS	-2.3		3.9
40	Tabeja	TJ1	purple fluorite	FIA2	fi8	spherical	10	aqueous, 2phase	growth zone	primary	Type 2	140	LV→L	-3.1		5.1
41	Tabeja	TJ1	purple fluorite	FIA2	fi9	negative crystal	18	aqueous, 2phase	growth zone	primary	Type 2	138	LV→L	-3.9		6.3
42	Tabeja	TJ1	purple fluorite	FIA2	fi10	spherical	40	aqueous, 3 phase	growth zone	primary	Type 2	125.8	LVS→LS	-3.5		5.7
43	Tabeja	TJ1	purple fluorite	FIA3	fi1	negative crystal	20	aqueous, 2phase	growth zone	primary	Type 2	122	LV→L	-3.1		5.1
44	Tabeja	TJ1	purple fluorite	FIA3	fi2	negative crystal	30	aqueous, 2phase	growth zone	primary	Type 2	118.1	LV→L	-2.9		4.8
45	Tabeja	TJ1	purple fluorite	FIA4	fi1	negative crystal	20	aqueous, 3 phase	growth zone	primary	Type 2	129.6	LVS→LS	-3.7		6.0
46	Tabeja	TJ1	purple fluorite	FIA4	fi2	negative crystal	18	aqueous, 3 phase	growth zone	primary	Type 2	133.9	LVS→LS	-3.7		6.0
47	Tabeja	TJ1	purple fluorite	FIA4	fi3	negative crystal	10	aqueous, 3 phase	growth zone	primary	Type 2	137.3	LVS→LS	-2.1		3.5
48	Bou Izourane	BZ1	banded purple-white fluorite	FIA1	fi1	equant	18	aqueous, 2phase	growth zone	primary	Type 2	134	LV→L	-3.2		5.3
49	Bou Izourane	BZ1	banded purple-white fluorite	FIA1	fi2	cylindrical	30	aqueous, 2phase	growth zone	primary	Type 2	132.8	LV→L	-3.8		6.2
50	Bou Izourane	BZ1	banded purple-	FIA1	fi3	irregular	30	aqueous, 2phase	growth zone	primary	Type 2	133.4	LV→L	-3.8	-38	6.2

			white fluorite banded purple-white													
51	Bou Izourane	BZ1	fluorite banded purple-white	FIA1	fi4	cubic	18	aqueous, 2phase	growth zone	primary	Type 2	135.5	LV→L	-2.8		4.6
52	Bou Izourane	BZ1	fluorite banded purple-white	FIA1	fi5	irregular	40	aqueous, 2phase	growth zone	primary	Type 2	131	LV→L	-3.5	-40	5.7
53	Bou Izourane	BZ1	fluorite banded purple-white	FIA1	fi6	equant	20	aqueous, 2phase	growth zone	primary	Type 2	132.5	LV→L	-2.6		4.3
54	Bou Izourane	BZ1	fluorite banded purple-white	FIA1	fi7	cubic	18	aqueous, 2phase	growth zone	primary	Type 2	132.2	LV→L	-3.3		5.4
55	Bou Izourane	BZ1	fluorite banded purple-white	FIA1	fi8	cubic	23	aqueous, 2phase	growth zone	primary	Type 2	130.7	LV→L	-3.4	-42	5.6
56	Bou Izourane	BZ1	fluorite banded purple-white	FIA1	fi9	irregular	20	aqueous, 2phase	growth zone	primary	Type 2	133.7	LV→L	-3.4	-39	5.6
57	Bou Izourane	BZ1	fluorite banded purple-white	FIA1	fi10	cylindrical	12	aqueous, 2phase	growth zone	primary	Type 2	133.1	LV→L	-2.3		3.9
58	Bou Izourane	BZ9	fluorite banded purple-white	FIA1	fi1	negative crystal	30	aqueous, 2phase	growth zone	primary	Type 2	129.9	LV→L	-4.1	-32	6.6
59	Bou Izourane	BZ9	fluorite banded purple-white	FIA1	fi2	negative crystal	20	aqueous, 2phase	growth zone	primary	Type 2	137.2	LV→L	-2.7		4.5
60	Bou Izourane	BZ9	fluorite banded purple-white	FIA1	fi3	negative crystal	15	aqueous, 2phase	growth zone	primary	Type 2	134	LV→L	-3	-36	5.0
61	Bou Izourane	BZ9	fluorite banded purple-white	FIA1	fi4	negative crystal	15	aqueous, 2phase	growth zone	primary	Type 2	136.4	LV→L	-3		5.0
62	Bou Izourane	BZ9	fluorite banded purple-white	FIA1	fi5	negative crystal	12	aqueous, 2phase	growth zone	primary	Type 2	136.5	LV→L	-3.8		6.2
63	Bou Izourane	BZ9	fluorite banded purple-white	FIA1	fi1	prismatic	30	aqueous, 2phase	growth zone	primary	Type 2	124.4	LV→L	-1	-27	1.7
64	Bou Izourane	BZ9	fluorite	FIA1	fi2	prismatic	15	aqueous, 2phase	growth zone	primary	Type 2	135.5	LV→L	-0.9		1.6

65	Bou Izourane	BZ9	banded purple-white fluorite	FIA1	fi3	cylindrical	15	aqueous, 2phase	growth zone	primary	Type 2	134.4	LV→L	-1	1.7
66	Bou Izourane	BZ9	banded purple-white fluorite	FIA2	fi1	cubic	10	aqueous, 2phase	trail within growth zone	pseudo-secondary	Type 3	303	LV→L	-0.8	1.4
67	Bou Izourane	BZ9	banded purple-white fluorite	FIA2	fi2	cylindrical	12	aqueous, 2phase	trail within growth zone	pseudo-secondary	Type 3	315	LV→L	-0.4	0.7
68	Bou Izourane	BZ9	banded purple-white fluorite	FIA2	fi3	cubic	8	aqueous, 2phase	trail within growth zone	pseudo-secondary	Type 3	307	LV→L	-0.3	0.5
69	Bou Izourane	BZ9	banded purple-white fluorite	FIA2	fi4	cylindrical	10	aqueous, 2phase	trail within growth zone	pseudo-secondary	Type 3	314	LV→L	-0.5	0.9
70	Bou Izourane	BZ9	banded purple-white fluorite	FIA2	fi5	cylindrical	10	aqueous, 2phase	trail within growth zone	pseudo-secondary	Type 3	317	LV→L	-0.5	0.9
71	Bou Izourane	BZ9	banded purple-white fluorite	FIA2	fi6	cubic	8	aqueous, 2phase	trail within growth zone	pseudo-secondary	Type 3	307	LV→L	-0.5	0.9
72	Bou Izourane	BZ9	banded purple-white fluorite	FIA2	fi7	negative crystal	8	aqueous, 2phase	trail within growth zone	pseudo-secondary	Type 3	317	LV→L	-0.6	1.1
73	Bou Izourane	BZ9	banded purple-white fluorite	FIA3	fi1	negative crystal	12	aqueous, 2phase	trail within growth zone	pseudo-secondary	Type 3	302	LV→L		
74	Bou Izourane	BZ9	banded purple-white fluorite	FIA3	fi2	cubic	10	aqueous, 2phase	trail within growth zone	pseudo-secondary	Type 3	335	LV→L	-0.4	0.7
75	Bou Izourane	BZ9	banded purple-white fluorite	FIA3	fi3	negative crystal	9	aqueous, 2phase	trail within growth zone	pseudo-secondary	Type 3	339	LV→L	-0.5	0.9
76	Bou Izourane	BZ6	banded purple-white fluorite	FIA1	fi1	negative crystal	18	aqueous, 2phase	plane within growth zone	pseudo-secondary	Type 3	252	LV→L	-1.4	2.4
77	Bou Izourane	BZ6	banded purple-white fluorite	FIA1	fi2	spherical	10	aqueous, 2phase	plane within growth zone	pseudo-secondary	Type 3	250	LV→L	-1.1	1.9
78	Bou Izourane	BZ6	banded purple-white fluorite	FIA1	fi3	cylindrical	20	aqueous, 2phase	plane within growth zone	pseudo-secondary	Type 3	244	LV→L	-1.3	2.2
79	Bou Izourane	BZ6	banded purple-	FIA1	fi4	negative crystal	5	aqueous, 2phase	plane within growth zone	pseudo-secondary	Type 3	233	LV→L	-1.6	2.7

80	Bou Izourane	BZ6	white fluorite banded purple-white fluorite	FIA1	fi5	cylindrical	10	aqueous, 2phase	plane within growth zone	pseudo-secondary	Type 3	248	LV→L	-1.3		2.2
81	Bou Izourane	BZ6	purple-white fluorite banded purple-white fluorite	FIA1	fi6	cubic	6	aqueous, 2phase	plane within growth zone	pseudo-secondary	Type 3	218	LV→L	-1.7		2.9
82	Bou Izourane	BZ6	purple-white fluorite banded purple-white fluorite	FIA1	fi7	spherical	6	aqueous, 2phase	plane within growth zone	pseudo-secondary	Type 3	246	LV→L	-1.8		3.1
83	Bou Izourane	BZ6	purple-white fluorite banded purple-white fluorite	FIA1	fi8	cubic	8	aqueous, 2phase	plane within growth zone	pseudo-secondary	Type 3	261	LV→L	-1.4		2.4
84	Bou Izourane	BZ6	white fluorite	FIA1	fi9	spherical	5	aqueous, 2phase	plane within growth zone	pseudo-secondary	Type 3	259	LV→L	-1.2		2.1
85	Bou Izourane	BZ3	white fluorite	FIA1	fi4	cylindrical	65	aqueous, 2phase	growth zone	primary	Type 2	130	LV→L			
86	Bou Izourane	BZ3	white fluorite	FIA1	fi8	prismatic	40	aqueous, 2phase	growth zone	primary	Type 2	130.3	LV→L			
87	Bou Izourane	BZ3	white fluorite	FIA1	fi5	irregular	40	aqueous, 2phase	growth zone	primary	Type 2	134.3	LV→L	-4		6.4
88	Bou Izourane	BZ3	white fluorite	FIA2	fi1	irregular	65	aqueous, 2phase	growth zone	primary	Type 2	139.6	LV→L	-3.6		5.9
89	Bou Izourane	BZ3	white fluorite	FIA2	fi2	cylindrical	30	aqueous, 2phase	growth zone	primary	Type 2	142.3	LV→L	-4		6.4
90	Bou Izourane	BZ3	white fluorite	FIA2	fi3	cylindrical	25	aqueous, 2phase	growth zone	primary	Type 2	143.2	LV→L	-4.7		7.4
91	Bou Izourane	BZ3	white fluorite	FIA2	fi6	cylindrical	20	aqueous, 2phase	growth zone	primary	Type 2	142.7	LV→L			
92	Bou Izourane	BZ3	white fluorite	FIA2	fi7	cylindrical	20	aqueous, 2phase	growth zone	primary	Type 2	143	LV→L	-3.8		6.2
93	Bou Izourane	BZ3	white fluorite	FIA2	fi9	irregular	20	aqueous, 2phase	growth zone	primary	Type 2	143.8	LV→L	-3.5		5.7
94	Bou Izourane	BZ3	white fluorite	FIA1	fi1	cylindrical	22	aqueous, 2phase	growth zone	primary	Type 2	145.8	LV→L	-5.5	-35	8.5
95	Bou Izourane	BZ3	white fluorite	FIA1	fi2	cylindrical	12	aqueous, 2phase	growth zone	primary	Type 2	141.5	LV→L	-4		6.4
96	Bou Izourane	BZ3	white fluorite	FIA1	fi3	cubic	5	aqueous, 2phase	growth zone	primary	Type 2	135.4	LV→L	-5.2		8.1
97	Bou Izourane	BZ3	white fluorite	FIA1	fi4	equant	8	aqueous, 2phase	growth zone	primary	Type 2	131.8	LV→L	-4.4		7.0
98	Bou Izourane	BZ5	white fluorite	FIA1	fi1	prismatic	20	aqueous, 2phase	growth zone	primary	Type 2	143.8	LV→L	-2		3.4
99	Bou Izourane	BZ5	white fluorite	FIA1	fi2	spherical	10	aqueous, 2phase	growth zone	primary	Type 2	153.7	LV→L	-2.9		4.8
100	Bou Izourane	BZ5	white fluorite	FIA1	fi3	cylindrical	30	aqueous, 2phase	growth zone	primary	Type 2	141.9	LV→L	-2.9		4.8
101	Bou Izourane	BZ5	white fluorite	FIA1	fi4	cylindrical	10	aqueous, 2phase	growth zone	primary	Type 2	151	LV→L	-3.1		5.1
102	Bou Izourane	BZ5	white fluorite	FIA1	fi5	cylindrical	10	aqueous, 2phase	growth zone	primary	Type 2	144.6	LV→L	-3.2		5.3

103	Bou Izourane	BZ5	white fluorite	FIA1	fi6	equant	8	aqueous, 2phase	growth zone	primary	Type 2	155.3	LV→L	-3.1	5.1